

Position Paper

Capturing sub-grid temperature and moisture variations for wildland fire modeling

Ginny A. Marshall^{a,b,*}, R.R. Linn^c, M. Holmes^c, S. Goodrick^d, D.K. Thompson^e, A. Hemmati^b^a Canadian Forest Service, Northern Forestry Centre, Edmonton, T6H 3S5, Canada^b University of Alberta, Edmonton, T6G 2R3, Canada^c Los Alamos National Laboratory, Earth and Environmental Science Division, Los Alamos, 87545, USA^d US Forest Service, Southern Research Station, GA, 30602, USA^e Canadian Forest Service, Great Lakes Forestry Centre, Sault Ste. Marie, P6B 2E5, Canada

ARTICLE INFO

Keywords:

Multiphysics modeling
Wildfire
Subgrid
Closure

ABSTRACT

Many wildfire behavior modeling studies have focused on fires during extreme conditions, where the dominant processes are resolved and smaller-scale variations have less influence on fire behavior. As such, wildfire behavior models typically perform well for these cases. However, they can struggle in marginal conditions (e.g. low-intensity fire) as small-scale variations significantly influence fire physics at scales below grid resolution. In an effort to generalize wildfire behavior models and improve their overall performance, we have developed a new set of equations for wet and dry fuel to capture the finer-scale sub-grid variations in temperature and moisture. We explore the behavior of these equations in simple scenarios ranging from high- to low-intensity fire. Furthermore, we evaluate the performance against observations of surface fire. In all cases the proposed model performs well after peak temperature is reached; however, the rise of fuel temperature at the onset of combustion is faster than expected.

1. Introduction

Wildfire behavior and spread is influenced by many complex processes, such as the exchange of mass, momentum, and energy through non-linear convective and radiative heating and cooling, combustion, and turbulence (Linn, 1997; Mell et al., 2007; Linn et al., 2002; Mell et al., 2009; Accary et al., 2014). These interactions depend heavily on the dynamic and heterogeneous turbulent flow fields that connect fire to its environment, including the surrounding atmosphere, fuels (dead and live vegetation) and topography. Current physics-based fire behavior models leverage computational fluid dynamics (CFD) techniques to represent the coupled fire-atmosphere interaction using partial differential equations (Linn, 1997; Mell et al., 2007; Morvan et al., 2018). An overview of fire models can be found in Sullivan (2009). Since fires (both wildfires and prescribed) occur at large spatial scales (hundreds of meters to hundreds of kilometers) and involve complex non-linear processes occurring at a wide variety of scales (e.g. atmospheric eddies hundreds of meters wide and reactions occurring in millimeter-diameter conifer needles), it is not currently feasible to resolve important phenomena over all these scales. Thus, in order to simulate wildland fires at landscape scales (100s of meters to kilometers or larger), compromises on resolution must be made

to offset computational limitations in large study areas (Linn et al., 2002; Linn and Cunningham, 2005a). As cell sizes increase, physics-based models are unable to resolve fine-scale, sub-grid processes and variations that have non-negligible influences, thus parameterizations must be developed to capture the net or aggregated effects of sub-grid phenomena. This need is analogous to the development of turbulence closure models that capture the net effects of variations in a flow field that cannot be resolved.

Recent CFD-based wildfire studies have focused on understanding the behavior of high-intensity wildfire scenarios (e.g. Hoffman et al., 2015, 2016; Marshall et al., 2020; Banerjee et al., 2020; Banerjee, 2020; Frangieh et al., 2018). These cases pose significant risks to people, communities, and infrastructure and are the most challenging to manage and suppress (Martell, 2001). The characteristic length scales of dominant fire phenomena (e.g. flame length) and fire geometry (e.g. fireline depth) typically increases with intensity of the fire (Byram, 1959). Simultaneously, the sensitivity of fires to fine-scale variations in the ambient environment (e.g. turbulence or fuel heterogeneity) and the impact of fine-scale variations in fire conditions (e.g. temperature or moisture variations) decreases with the increase in the characteristic length scales. When environmental conditions are conducive to extreme

* Corresponding author at: Canadian Forest Service, Northern Forestry Centre, Edmonton, T6H 3S5, Canada.

E-mail address: ginny.marshall@nrcan-rncan.gc.ca (G.A. Marshall).

<https://doi.org/10.1016/j.envsoft.2023.105678>

Received 11 July 2022; Received in revised form 8 February 2023; Accepted 8 March 2023

Available online 20 March 2023

1364-8152/© 2023 The Authors. Published by Elsevier Ltd. This is an open access article under the CC BY license (<http://creativecommons.org/licenses/by/4.0/>).



Fig. 1. Conceptual examples of (a) length scales in high intensity fire and (b) length scales and cell level heterogeneity in low intensity fire within a single computational grid cell.

Source: Figure (a) photo credit: Rex Hsieh, FPInnovations taken at Pelican Mountain (Thompson et al., 2020) and Figure (b) photo credit: Ginny Marshall, Natural Resources Canada.

fire (i.e., hot, dry and windy Potter and McEvoy, 2021) and fires are intense, existing physics-based wildfire behavior models are typically able to appropriately capture fire spread and fire intensity (e.g. Hoffman et al., 2016) since the dominating processes can generally be resolved and the impacts of sub-grid heterogeneities in temperature, wind, turbulence, fuel and moisture are less significant. An example of fire and fuel within a single computational cell for high intensity fire is shown in Fig. 1a. However, during lower-intensity fires, the spatial scales of fire behavior are smaller and the importance of finer-scale variations in fire activity and fire environment is greater than during high-intensity fire (Jonko et al., 2021; Linn et al., 2021; Parsons et al., 2011; Zhou et al., 2005). As the relevant length scales (e.g. flame length) of the fire decrease to below model resolution, physical wildfire behavior models struggle as a greater fraction of the critical fire-behavior-determining processes cannot be explicitly captured and must be captured by subgrid models (Linn, 1997; Veynante and Vervisch, 2002; Im et al., 1997). For example, there can be significant heterogeneity in temperatures of both gases and solids within unresolved volumes under these marginal conditions (hotter and cooler regions with respect to the mean resolved temperature) as is illustrated in Fig. 1b. Capturing the influences of this heterogeneity is important as it directly relates to the drying and combustion processes and thus the spread of fires. With increasing desire to consider the ecological effects of fires, the role of flanking and backing fires, and the use of prescribed fires, the importance of representing low intensity fires is increasing.

Physics-based coupled fire atmosphere models, such as FIRETEC (Linn, 1997; Linn et al., 2002), use a series of coupled partial differential equations to track the evolution of mass, momentum, energy, turbulence and species of gases moving around a fire, and the mass, moisture content, and temperature of the fuel (dead and live vegetation). In FIRETEC, as well as other similar models such as the Wildland Fire Dynamics Simulator (WFDS; Mell et al., 2007, 2009), the solution of these coupled partial differential equations is done numerically on a three-dimensional grid. Typical grid sizes for simulations with kilometer-scale domains is on the order of meters for both FIRETEC and WFDS. The temperature and moisture variations that govern some ignition and drying processes can thus be explicitly resolved on meter scales, but even at sub-meter scales there can be distributions of temperatures and moisture contents. Currently, FIRETEC employs the notion of a probability distribution function (PDF) of temperatures within each grid cell to determine the moisture evaporation and combustion rates. Using this approach, FIRETEC avoids having a step function in the rate of evaporation or combustion associated with the mean temperatures reaching critical values such as evaporation and

combustion temperatures. Instead, by accounting for the existence of a distribution of temperatures allows for a crude representation of the fact that a small fraction of the fuel might be hot enough to evaporate water or begin to combust. This approach has shown promise for some high-intensity fire scenarios based on model agreement with observations. However, the current formulation, which assumes a static subgrid temperature distribution shape, still presents challenges for low-intensity fire due to the significance of the sub-grid temperature variations which is greater than in high-intensity fire scenarios. For example, during high-intensity fire, which is characterized by highly turbulent flow and mixing (Clements et al., 2008; Seto et al., 2013; Clements and Seto, 2015; Clark et al., 2020), and flame lengths much larger than a single cell, the entire control volume (computational cell) would be relatively well mixed after the flame front has moved through the cell and combustion will occur in most (if not all) the fuel. In these cases, the cell size is small relative to the size of the flames and fireline depth. Conversely, during low-intensity fire, where flame lengths are much smaller than the cell and mixing is much lower, there can be regions of cool unburned fuel, regions of hot burning fuels, and regions of burned cooling fuel (Desai et al., 2021). As the importance of fine-scale variations increases with decreasing physical scales of the fires (lower intensity), the need for a more dynamic and scenario-dependent representation of the distributions of sub-grid variations increases.

The current FIRETEC formulation explicitly tracks a mean solid fuel temperature and allows an assumed temperature variance. The combination is used to determine how much of the fuel is hot enough to evaporate water and to begin combusting as the temperature of the mean fuel increases. For example, by including the notion of the distribution of temperatures within a cell (some hot locations and some that might be still at ambient) water can start being evaporated in some hot regions while the temperature is still at ambient levels in other parts of the cell. What is missing in the current/original formulation is scenario-dependent methodology for determining the width of the distribution, which will be determined by environmental factors such as wind speed, gas temperature variation, and even initial moisture content levels. Furthermore, the current formulation does not distinguish between wet fuels and dry fuels individually, but instead tracks only a single fuel mean fuel with a dynamic average moisture content. In reality, simultaneous processes could occur within a control volume, in which water evaporates from wet fuel to produce dry fuels, while at the same time, dry fuels may be subject to pyrolysis and combustion. In lower-intensity fire regimes, where the coincidence of drying and combustion occurring in the same cell increases, it is challenging to represent the influences of temperature distributions with a single energy equation for the solid fuel.

In an effort to improve the representation of subgrid processes related to temperature and moisture variation within a computational cell, we are working as part of a larger research initiative toward the implementation of a new set of equations describing the evolution of the variation of gas temperatures and both wet and dry solid temperatures. Particularly in this manuscript, however, we develop and propose a new set of equations that incorporate the conservation of mass and energy for the dry and wet fuels, individually, to ensure the model can better represent sub-grid combustion and evaporation processes simultaneously. This sets the first step towards completing our larger research initiative. To this end, the current manuscript is structured such that we outline the derivation of these new equations in Section 2, followed by a description of the proof of concept simulations in Section 3. We then present the results from a set of simple scenarios in Section 4. Main conclusions are presented in Section 5.

2. Model formulation

2.1. Equations for temperature of wet and dry fuel

Critical processes governing the spread of wildland fire depend on the temperature of the combustible material. In most natural scenarios the fuel is initially a combination of combustible biomass and water. The amount of water in the fuel is expressed as the fuel moisture fraction, which we define in the context of this manuscript as the mass of water divided by the mass of the oven-dried combustible biomass (or moisture content which is the moisture fraction written as a percent). This fuel moisture influences the temperature dynamics of combustible material because it adds significant thermal mass to the fuel and adds an energy sink associated with the evaporation of water. The initial water content of live fuels depends largely on plant physiological processes, which respond to a variety of environmental factors, such as seasonality, and available water in the ground (Jolly et al., 2014). The ambient water content of the dead fuel is a dynamic quantity that depends on the history of the local humidity and the size and shape of the biomass. Fine fuels equilibrate with the atmospheric moisture levels rapidly (<1 h), whereas thicker fuels take 10s, 100s or even thousands of hours to equilibrate (van der Kamp et al., 2017). Since wildland fire spread is heavily dependent on the fine fuels such as foliage, grasses or twigs our attention is currently focused on the dynamic conditions of this subset of the biomass, but future work will be needed to include larger fuels in this formulation as they are important for determining fire emissions, fire effects, and the sustaining of ignitions.

An equation for the evolution of the temperature of the solid (combustible fuel and associated water content) at a single point can be achieved by beginning with the equation for the conservation of internal energy of the solid (Linn, 1997). Then we subtract the conservation of mass equation multiplied by the temperature of the solid, T_s , and specific heat, c_{p_s} , which is a mass-weighted specific heat capacity of the combined wood ($c_{p_f} = 2500 \text{ J kg}^{-1} \text{ K}^{-1}$) and water ($c_{p_{\text{water}}} = 4200 \text{ J kg}^{-1} \text{ K}^{-1}$). For this purpose, the temperature of the biomass and water content are assumed to be the same value since the fuels are thermally and moisture thin. Equations of this sort are currently used in physics-based wildland fire models such as FIRETEC, as is shown in Eq. (1) (Linn et al., 2002; Linn and Cunningham, 2005b). In this equation, the bulk density of the solid, ρ_s , is treated as the sum of the bulk density of water, $\rho_{\text{H}_2\text{O}}$, and fuel, ρ_f . The combined internal energy of the fuel and water is the product of ρ_s , T_s , and the mass-weighted specific heat, c_{p_s} .

$$c_{p_s} \rho_s \frac{\partial T_s}{\partial t} = q + h a_v (T_g - T_s) + F_f (H_f \Theta - c_{p_f} T_{\text{crit}} N_f) - F_{\text{H}_2\text{O}} (H_{\text{H}_2\text{O}} + c_{p_{\text{H}_2\text{O}}} T_{\text{vap}}) \quad (1)$$

In Eq. (1), t is time, q is the net radiation heat transfer rate per unit volume, h is the convective heat transfer coefficient, a_v is the area

per unit volume of the fuel in a cell, T_g is the local temperature of the gas, F_f is the mixing-limited reaction rate as described by Linn (1997), H_f is the heat of combustion of the fuel, Θ is the fraction of the reaction energy that is deposited directly back to the fuel, T_{crit} is a critical local temperature for pyrolysis (taken to be 600 K in this manuscript, which is consistent with the critical temperature currently used in FIRETEC), N_f is a stoichiometric coefficient for the net burning reaction as described by Drysdale (1985), $F_{\text{H}_2\text{O}}$ is the rate of water evaporation, $H_{\text{H}_2\text{O}}$ is the heat of vaporization of liquid water, and T_{vap} is the temperature of water vaporization at standard pressure. For a single location, $F_{\text{H}_2\text{O}}$ only has a non-zero value when the temperature of that location is T_{vap} and above this temperature the moisture content is zero. F_f begins (is non-zero) at the critical temperature, but it can persist at higher temperatures since combustion depends on other factors, such as oxygen concentration and mixing.

There are challenges associated with applying this equation in numerical simulations, where computations are not performed at every single point but are instead used to describe the mean temperature in a control volume or computational cell. In the case of models designed for landscape-scale fires, length scales in these control volumes can be on the order of meters. In such volume sizes, there can be a mixture of states (e.g. distribution of temperatures and a mixture of fuels that are wet and have begun drying) that are not explicitly resolved (Linn, 1997). For example, it is possible to have fuel that is wet, drying, dried and heating up, and combusting all in the same computational cell, especially in the context of low-intensity fires. In an attempt to account for the fact that there was likely a range of temperatures within the control volume, the concept of temperature distribution or PDF was introduced (Linn, 1997) in the reaction rate and later to the moisture evaporation. This concept, which captures the presence of both warm and cold fuel within a volume, allowed moisture to begin to evaporate before the mean temperature reached vaporization temperature and for combustion to start even before all of the moisture was evaporated. In the original implementation of FIRETEC (Linn, 1997; Linn et al., 2002), however, there was no mechanism that allowed for the PDF width or shape to dynamically evolve based on the fire environment (i.e., the distribution is fixed and does not evolve and adapt). This presents challenges to the generality of the model and its applicability to portions of low-intensity fire since it cannot be assumed that the distribution is universal in all fire-scenarios.

In order to increase the generality (flexibility or range of scenarios that are applicable) of this approach, it is necessary to incorporate a dynamic PDF that adapts to the fire environment. During the development of the original formulations (Linn, 1997) and subsequent model improvement efforts, attempts to derive the governing equations for the dynamic width, or standard deviation, of the PDF for the solid temperature distribution ran into challenges related to the phase change threshold associated with moisture evaporation. The equations for a variance of the temperature distribution were tractable for temperatures above and below the temperature of evaporation. In this original formulation, the amount of moisture associated with the fuel was tracked and one could back out the fraction of the solid that was wet and dry, but it was not possible to track the temperature of the wet and dry components separately and thus it was difficult to estimate the fraction of the fuel that was hot enough to combust and the fraction that still had moisture to evaporate. Thus, in order to better track the distribution of temperatures, the evaporation of water, and the potentially simultaneous combustion processes that occur within a control volume, we propose a new alternative approach to capture the evolution of wet and dry solids.

For this newly proposed approach, we partition the solid fuel into two categories or states; wet and dry. The wet fuel is the biomass that has the initial moisture content (determined by the ambient conditions pre-fire) and dry fuel is the biomass that has had the moisture driven off as a result of heating by the fire. Using this construct, the bulk density of the fuel-moisture mixture, ρ_s , is the sum of dry fuel, ρ_d , and wet fuel,

ρ_w , and water, ρ_{H_2O} . This is illustrated in Eq. (2), where wet fuel and water can be combined to obtain the bulk density of the wet solid, that is $\rho_{sw} = \rho_w + \rho_{H_2O}$,

$$\rho_s = \rho_d + \rho_w + \rho_{H_2O} = \rho_d + \rho_{sw}. \quad (2)$$

The conceptual division between the wet and dry fuel is based on the notion that fuel is initially wet and then it is dried to generate dry fuel. We assume that all fuel within a control volume has the same initial moisture fraction, or ratio, r_{moist} ($r_{moist} > 0$), which remains constant for the wet fuel. While it is possible to have multiple fuels with differing moisture contents co-existing within a single cell, for simplicity we adopt only one representative fuel with a single moisture fraction. Additionally, the moisture fraction of the wet fuel remains constant since the water evaporation in a fuel particle results in the creation of dry fuel (and consistent removal of wet fuel). Thus, we are tracking moisture in the cell through the shifting mass balance of wet fuels, which remain at the initial moisture level, and dry fuels, which always have zero moisture. The total moisture fraction of the cell (mass-weighted average moisture combining wet and dry fuel components) will evolve and decrease with evaporation. Furthermore, there is initially no dry fuel since even dead fuels (e.g. dry needles and dried grass) have a non-zero equilibrium moisture content with the atmospheric humidity (even in extremely dry conditions dead fuel moistures are typically above 0.03 or higher, however, moistures can be as low as 0.01 or lower (Aguado et al., 2007)). Thus, the bulk density of the wet solid is the same as the bulk density of the solid, $\rho_{sw} = \rho_s$, at the initialization.

With this in mind, the conservation of mass equations for the water and the wet fuel based on the rate of evaporation of water per unit volume, F_{H_2O} , are:

$$\frac{\partial \rho_{H_2O}}{\partial t} = -F_{H_2O} \quad (3)$$

$$\frac{\partial \rho_w}{\partial t} = -\frac{F_{H_2O}}{r_{moist,w}} \quad (4)$$

where the moisture fraction of the wet solid is given by:

$$r_{moist,w} = \frac{\rho_{H_2O}}{\rho_w}. \quad (5)$$

The term $r_{moist,w}$ must be greater than zero since the wet solid fuel will never be completely dry, but $r_{moist,w}$ can be larger than one which simply indicates that the mass of the water is larger than the mass of the biomass. For example, a live deciduous leaf could have a moisture fraction of 2, meaning the mass of water contained in the leaf is twice that of the dry mass.

We assume that ρ_{H_2O} approaches zero at a rate proportional to the rate that wet mass becomes dry. Thus, $r_{moist,w}$ remains a constant even when water is completely evaporated. We can then form the conservation of mass of the wet solid and its moisture, ρ_{sw} :

$$\frac{\partial \rho_{sw}}{\partial t} = -F_{H_2O} \left(1 + \frac{1}{r_{moist,w}} \right), \quad (6)$$

where mass loss from the wet fuel conservation equation corresponds to a mass source in the conservation of dry fuel equation:

$$\frac{\partial \rho_d}{\partial t} = -F_f N_f + \frac{F_{H_2O}}{r_{moist,w}}. \quad (7)$$

The additional sink term in Eq. (7), $-F_f N_f$, corresponds to the mass loss rate due to the burning of dry fuel. Using the definition of the two different categories of solids, we can then write conservation equations for the internal energy of both wet and dry solids respectively,

$$\begin{aligned} \frac{\partial c_{p_{sw}} \rho_{sw} T_w}{\partial t} = & q_w + h a_{v,sw} (T_g - T_w) + F_f H_f \Theta_w \\ & - F_{H_2O} \left(c_{p_{H_2O}} + \frac{c_{p_f}}{r_{moist,w}} \right) T_{vap} - F_{H_2O} H_{H_2O} \end{aligned} \quad (8)$$

and

$$\begin{aligned} \frac{\partial c_{p_f} \rho_d T_d}{\partial t} = & q_d + h a_{v,d} (T_g - T_d) + F_f H_f \Theta_d \\ & + F_{H_2O} \frac{c_{p_f}}{r_{moist,w}} T_{vap} - F_f N_f c_{p_f} T_{combust} \end{aligned} \quad (9)$$

where $c_{p_{sw}} \rho_{sw} = \rho_{H_2O} c_{p_{H_2O}} + c_{p_f} \rho_w$, $c_{p_{sw}}$ is the mass weighted specific heat capacity of the wet fuel, T_d is the dry fuel temperature, T_w is the wet fuel temperature, T_g is the gas phase temperature, Θ_w and Θ_d are the fraction of combustion energy that is directly deposited on the wet and dry solid respectively, $T_{combust}$ is the temperature at which combustion occurs and solid fuel mass is converted to gaseous products, and h is the convective heat transfer coefficient, which is assumed to be the same for wet and dry materials given they are the same shape and size. $a_{v,sw}$ and $a_{v,d}$ are the area per unit volume of the wet and dry fuel, which are calculated based on their respective bulk density, ρ_x , the material density, ρ_{micro} , and size scale (radius of cylindrical fuel particles), s_x , of the fuel particles:

$$a_{v,x} = \frac{2\rho_x}{s_x \rho_{micro}} \quad (10)$$

where the subscript x indicates either wet fuel (abbreviated sw) or dry fuel (abbreviated d) bulk density.

In both Eqs. (8) and (9), the first terms on the right side of the equation are net radiation, the second terms are convective heat transfer, and the third terms are deposition of energy deposited via the combustion processes. The fourth terms on the right side of these equations represent the transfer of energy associated with the movement of mass from the wet state to the dry state and the loss of the mass of the water from the wet state. The final terms in the wet internal energy equation (Eq. (8)) represents the endothermic evaporation process. It is important to note that the evaporation rate goes to zero as the density of wet fuel goes to zero. The final term in the dry internal energy equation (Eq. (9)) accounts for energy loss from the dry state due to the mass losses associated with gaseous products in the combustion process.

Since the wet fuel temperatures are expected to change less than 100 K and the moisture fraction of this fuel is held fixed at the initial level, we treat the specific heat of the wet fuel as constant throughout the simulation. Thus, we can subtract the product of the specific heat, the temperature of wet fuel, and the conservation of wet mass equation (Eq. (6)), that is

$$c_{p_{sw}} T_w \frac{\partial \rho_{sw}}{\partial t} = -F_{H_2O} \left(c_{p_{H_2O}} + \frac{c_{p_f}}{r_{moist,w}} \right) T_w, \quad (11)$$

from Eq. (8), to arrive at:

$$\begin{aligned} c_{p_{sw}} \rho_{sw} \frac{\partial T_w}{\partial t} = & q_w + h a_{v,sw} (T_g - T_w) + F_f H_f \Theta_w - F_{H_2O} H_{H_2O} \\ & + F_{H_2O} \left(c_{p_{H_2O}} + \frac{c_{p_f}}{r_{moist,w}} \right) (T_w \delta_{wet} - T_{vap}). \end{aligned} \quad (12)$$

In Eq. (12), δ_{wet} (defined in Eq. (13)) has been added to account for the fact that water evaporation only occurs when $T_w = T_{vap}$, which means that $F_{H_2O} \neq 0$ when the wet solid temperature is T_{vap} . Thus, the final F_{H_2O} term will cancel since we assume there is no evaporation when the temperature is below T_{vap} , and when any portion of the wet fuel reaches T_{vap} , the water is immediately evaporated (assuming standard pressure). The newly dried fuel is now tracked in the dry fuel equation.

$$\delta_{wet} = \begin{cases} 0, & T_w < T_{vap} \\ 1, & T_w = T_{vap} \end{cases} \quad (13)$$

For the dry fuels, we similarly subtract the term $c_{p_f} T_d \frac{\partial \rho_d}{\partial t}$, defined as:

$$c_{p_f} T_d \frac{\partial \rho_d}{\partial t} = -c_{p_f} T_d F_f N_f + c_{p_f} T_d \frac{F_{H_2O}}{r_{moist,w}} \quad (14)$$

from Eq. (9). Thus, we arrive at:

$$c_{p_f} \rho_d \frac{\partial T_d}{\partial t} = q_d + h a_{v,d} (T_g - T_d) + F_f H_f \Theta_d + \frac{F_{H_2O}}{r_{moist,w}} c_{p_f} (T_{vap} - T_d) + F_f N_f c_{p_f} (T_d \delta_{dry} - T_{combust}). \quad (15)$$

Analogous to δ_{wet} in the wet temperature equation, δ_{dry} is added, that is

$$\delta_{dry} = \begin{cases} 0, & T_d \neq T_{combust} \\ 1, & T_d = T_{combust} \end{cases} \quad (16)$$

Thus, the last two terms in Eq. (15) now cancel each other. It is worth noting that $T_{combust}$ is not a fixed value, but it is the temperature at which combustion is taking place at any given location or instant.

The concept of wet and dry fuel for this formulation is associated with wet and dry fuel particles or even wet and dry sections of length of fuel particles in the case of thin fuels, which is our focus here. In future formulations, this can be expanded to handle gradients of moisture within thicker fuels as the outer shell can be dried while the inner core might still be wet. For the current case, however, we only considered the case of thermally thin and moisture thin fuels, which constitutes homogeneous temperatures and moisture fraction throughout the fuel particle thickness. In development of a new model, it is reasonable to start with the more simplified, but still realistic conditions, such as the one considered here. The areas per volume of the wet and dry mass, $a_{v,sw}$ and $a_{v,d}$, can be related to an aggregate area per volume. That is if we assume that the difference in wet versus dry fuel is predominantly due to position in the cell (i.e., one spot has been dried out, while another spot is still wet),

$$a_{v,sw} = a_v \frac{\rho_{sw}}{\rho_d + \rho_{sw}} \quad (17)$$

and

$$a_{v,d} = a_v \frac{\rho_d}{\rho_d + \rho_{sw}}. \quad (18)$$

This follows a reasonable observation that heating will begin on just one side of the cell as wind and turbulence initially advect and mix hot gases into the cell from one direction.

The fraction of combustion energy returning directly to the solid, Θ_s , can be split into a fraction that is deposited directly on the dry and wet fuels. In such a spatially segregated paradigm, however, we are in principle assuming that the energy returning to the solid is predominantly to the dry solid, where combustion is occurring. Thus, we approximate these terms as $\Theta_d = \Theta_s$ and $\Theta_w = 0$.

2.2. Mean temperature equations

To derive the equation for the mean temperatures of the wet and dry solids, we decompose the quantities of Eqs. (12) and (15) into mean (denoted by an overbar) and fluctuating parts (denoted with '). Then, we take the ensemble average of these equations similar to the development of mean velocity equations in turbulence modeling (Daly and Harlow, 1970). Thus, we get the following two expressions:

$$\begin{aligned} c_{p_f} \left(\bar{\rho}_d \frac{\partial \bar{T}_d}{\partial t} + \overline{\rho'_d \frac{\partial T'_d}{\partial t}} \right) &= \bar{q}_d + \bar{h} \bar{a}_{v,d} (\bar{T}_g - \bar{T}_d) + \bar{h} (\overline{a'_{v,d} T'_g} - \overline{a'_{v,d} T'_d}) \\ &\quad + \bar{a}_{v,d} (\overline{h' T'_g} - \overline{h' T'_d}) \\ &\quad + \overline{h' a'_{v,d} T'_g} - \overline{h' a'_{v,d} T'_d} \\ &\quad + \bar{F}_f (H_f \Theta_d) \\ &\quad + \bar{F}_{H_2O} \frac{c_{p_f}}{r_{moist,w}} [T_{vap} - \bar{T}_d] - \frac{c_{p_f}}{r_{moist,w}} \overline{F'_{H_2O} T'_d} \end{aligned} \quad (19)$$

$$\begin{aligned} c_{p_{sw}} \left(\bar{\rho}_{sw} \frac{\partial \bar{T}_w}{\partial t} + \overline{\rho'_{sw} \frac{\partial T'_w}{\partial t}} \right) &= \bar{q}_w + \bar{h} \bar{a}_{v,sw} (\bar{T}_g - \bar{T}_w) \\ &\quad + \bar{h} (\overline{a'_{v,sw} T'_g} - \overline{a'_{v,sw} T'_w}) \\ &\quad + \bar{a}_{v,sw} (\overline{h' T'_g} - \overline{h' T'_w}) \\ &\quad + \overline{h' a'_{v,sw} T'_g} - \overline{h' a'_{v,sw} T'_d} \\ &\quad + \bar{F}_f H_f \Theta_w - \bar{F}_{H_2O} H_{H_2O}. \end{aligned} \quad (20)$$

If we consider the solid density distribution or density variation to be somewhat dominated by the presence of, or the lack of, a fuel particle at a specific location and thus bimodal, then we can neglect $T'_d \rho'_d$ terms. This implies that both positive and negative dry fuel temperature fluctuations exist, where there is fuel (positive density fluctuation), and neither are relevant in locations where there is no dry fuel. We extend this argument to wet fuels as well. Additionally, if we assume that fuel particles do not change their radius while they burn, but rather shrink in their length (and local density) until they disappear, then the correlations between $a'_{v,d}$ and $a'_{v,sw}$ can be neglected. This approximation is consistent with previous work, in which the size scale of particles does not change with combustion, for example Linn (1997) and Linn et al. (2002). Thus, the correlations between $a'_{v,d}$ and temperature are minimal even if the radius was changing. It is also reasonable to assume changes in the heat transfer coefficient are not due to changing solid temperature, but rather due to properties of the air, i.e., temperature or velocity, since the heat transfer coefficient itself is a function of air properties (see Eq. (23)). As a first approximation, therefore, we assign $\overline{h' T'_d} = 0$ and $\overline{h' T'_w} = 0$. Finally, we neglect third and higher-order correlation terms for this initial approach at the dynamic PDF for simplicity.

With the above simplifications, we are left with the following expressions:

$$\begin{aligned} c_{p_f} \bar{\rho}_d \frac{\partial \bar{T}_d}{\partial t} &= \bar{q}_d + \bar{h} \bar{a}_{v,d} (\bar{T}_g - \bar{T}_d) + \bar{a}_{v,d} \overline{h' T'_g} + \bar{F}_f (H_f \Theta_d) \\ &\quad + \bar{F}_{H_2O} \frac{c_{p_f}}{r_{moist,w}} [T_{vap} - \bar{T}_d] - \frac{c_{p_f}}{r_{moist,w}} \overline{F'_{H_2O} T'_d} \end{aligned} \quad (21)$$

$$\begin{aligned} c_{p_{sw}} \bar{\rho}_{sw} \frac{\partial \bar{T}_w}{\partial t} &= \bar{q}_w + \bar{h} \bar{a}_{v,sw} (\bar{T}_g - \bar{T}_w) + \bar{a}_{v,sw} \overline{h' T'_g} \\ &\quad + \bar{F}_f H_f \Theta_w - \bar{F}_{H_2O} H_{H_2O}. \end{aligned} \quad (22)$$

These expressions are not in a closed form due to two terms: $\overline{h' T'_g}$ and $-\overline{F'_{H_2O} T'_d}$. We now try to address this closure problem. Beginning with the covariance between the heat transfer coefficient and the gas temperature, we first consider the equation for the heat transfer coefficient used in FIRETEC, that is

$$h = (0.25)(0.683) Re^{0.466} \frac{\lambda_{air}}{s_s}, \quad (23)$$

as was described by Incropera and DeWitt (1996) for forced convection over tubes with the local Reynolds number defined as:

$$Re = \frac{U s_s}{\nu}. \quad (24)$$

In these equations, λ_{air} is the thermal conductivity of air, U is the local velocity (including contributions from mean and fluctuating components), and ν is kinematic viscosity.

We utilize a simple linear relationship with gas temperature for both viscosity and conductivity, such that $\nu = C_1 T_g - C_2$ and $\lambda_{air} = C_3 T_g + C_4$, where $C_1 = 1.66 \times 10^{-7}$, $C_2 = 3.37 \times 10^{-5}$, $C_3 = 5.55 \times 10^{-5}$, and

$C_4 = 9.59 \times 10^{-3}$. Incorporating these new equations into Eq. (23) we arrive at

$$h = (0.25)(0.683) \left(\frac{U_{s_s}}{C_1 T_g - C_2} \right)^{0.466} \frac{C_3 T_g + C_4}{s_s}. \quad (25)$$

Formulating the convective heat transfer coefficient as a function of T_g allows us to determine $\frac{\partial h}{\partial T_g}$ and estimate the correlation $\overline{h'T'_g}$ using:

$$\overline{h'T'_g} = \frac{\partial h}{\partial T_g} \overline{T'_g T'_g}. \quad (26)$$

Based on the approximated equation for h , we find

$$\frac{\partial h}{\partial T_g} = \frac{(0.25)(0.683)(U)^{0.466}}{s_s^{0.534}} \left[\left(\frac{1}{C_1 T_g - C_2} \right)^{0.466} C_3 - (0.466) \frac{C_1}{(C_1 T_g - C_2)^{1.466}} (C_3 T_g + C_4) \right]. \quad (27)$$

The correlation between the fluctuations in water evaporation rate and the temperature of the dry fuel, that is $-\overline{F'_{H_2O} T'_d}$, is nonzero in the case where the mean dry temperature is above the temperature for vaporization and there is still additional mass being moved from wet to dry fuel state. In this scenario, a positive fluctuation in the evaporation (as the mean temperature of the wet fuel will always be less than the evaporation temperature) results in additional mass source for the dry fuel at a temperature lower than the mean dry temperature (a negative temperature fluctuation). If the evaporation rate is non-zero, but the mean dry temperature has fallen below the temperature for vaporization, we expect a positive fluctuation in the evaporation rate to coincide with a positive fluctuation in the dry temperature as we are adding dry fuel at a temperature that is higher than the current mean dry temperature. The correlation is expected to increase with the width of the distribution and scale with the mean evaporation rate. Thus, we model this correlation as

$$-\overline{F'_{H_2O} T'_d} = -\overline{F_{H_2O}} \sqrt{\frac{\overline{T'_d T'_d} - T_{vap}}{\overline{T_d}}}. \quad (28)$$

2.3. Equations for temperature variance

Evolution of the width of the probability density functions for the temperatures of the wet and dry solids within a volume is tracked based on a similar approach as the development of turbulence transport equations (Daly and Harlow, 1970). Similar to velocities and pressure in turbulence modeling, the quantities of Eq. (15) are decomposed into mean and fluctuating parts. Then, both sides of the equation are multiplied by the fluctuation of the temperature, followed by ensemble averaging of the entire equation. Starting with the dry temperature equation, this process results in the following expression:

$$\begin{aligned} c_{pf} \left(\overline{\rho'_d T'_d \frac{\partial T'_d}{\partial t}} + \overline{T'_d \rho'_d \frac{\partial T_d}{\partial t}} + \overline{T'_d \rho'_d \frac{\partial T'_d}{\partial t}} \right) \\ = \overline{T'_d q'_d} + \overline{h a_{v,d}} (\overline{T'_d T'_g} - \overline{T'_d T'_d}) \\ + \overline{h T'_d a'_{v,d}} (\overline{T_g} - \overline{T_d}) + \overline{h (a'_{v,d} T'_g T'_d - a'_{v,d} T'_d T'_d)} \\ + \overline{a_{v,d}} (\overline{T'_d h' T'_g} + \overline{T'_d h' T'_g} - \overline{T'_d h' T_d} - \overline{T'_d T'_d h'}) \\ + \overline{T'_d h' a'_{v,d}} (\overline{T_g} - \overline{T_d}) + \overline{T'_d h' a'_{v,d} T'_g} - \overline{T'_d h' a'_{v,d} T'_d} \\ + \overline{T'_d F'_f H_f \Theta_d} - \overline{F_{H_2O}} \frac{c_{pf}}{r_{moist,w}} \overline{T'_d T'_d} \\ + \frac{c_{pf}}{r_{moist,w}} \overline{F_{H_2O} T'_d} (\overline{T_{vap}} - \overline{T_d}) \\ - \frac{c_{pf}}{r_{moist,w}} \overline{F'_{H_2O} T'_d T'_d}. \end{aligned} \quad (29)$$

Rearranging Eq. (29) and applying the assumptions described above for the mean temperature equations, we arrive at an equation for the variance, $\overline{T'_d T'_d}$:

$$\frac{\partial \overline{T'_d T'_d}}{\partial t} = \frac{2}{c_{pf} \rho_d} \left[\overline{q'_d T'_d} + \overline{h a_{v,d}} (\overline{T'_d T'_g} - \overline{T'_d T'_d}) + \overline{T'_d F'_f H_f \Theta_d} + \frac{c_{pf}}{r_{moist,w}} \overline{F_{H_2O} T'_d} (\overline{T_{vap}} - \overline{T_d}) - \frac{c_{pf}}{r_{moist,w}} \overline{F_{H_2O} T'_d T'_d} \right]. \quad (30)$$

Here, we have three unknown terms: $\overline{q'_d T'_d}$, $\overline{T'_d T'_g}$, and $\overline{T'_d F'_f}$ that we need to address to close Eq. (30). The correlation between the evaporation rate and the dry temperature, $\overline{F'_{H_2O} T'_d}$, was discussed in the previous subsection.

For the correlation between radiation and dry temperature, $\overline{q'_d T'_d}$, we assume the net heat transfer will depend only on the energy emitted from the dry fuel. This is a simplification, but lab studies have shown (Cohen and Finney, 2022a,b) that in thermally thin fuels, convective heating plays a larger role in pre-heating the fuels, thus we omit radiative energy gains at this stage in development. Leveraging approaches used in variable density turbulence (Besnard et al., 1992) and the Stefan–Boltzmann law for blackbody radiation emission ($q_{emitted} = a_v \epsilon \sigma T^4$ (Incropera and DeWitt, 1996)), we can approximate the dependence of a perturbation of the emitted radiation on the temperature of the dry fuel with $q'_{emitted} = 4a_v \epsilon \sigma T'^3 T'$. In these equations, σ is the Stefan–Boltzmann constant, ϵ is emissivity, and we include an added view factor correction, γ , for scenarios where fuels are compacted in the bottom of a computational cell as is the case for litter or grass layer (the value of γ is 1 when the fuel is distributed throughout the cell). This view factor can be thought of as a correction on the area per unit volume. Since emitted radiation is a net negative radiation contribution, this term will act as a sink from the $\overline{T'_d T'_d}$ equation. Furthermore, neglecting a' terms due to the assumed constant radius of the fuel particle, we arrive at

$$\overline{q' T'_d} = -4a_{v,d} \epsilon \gamma \sigma \overline{T_d^3 T'_d T'_d}. \quad (31)$$

The correlation between the temperature of the dry fuel and the reaction rate, $\overline{T'_d F'_f}$, is important in cases where the mean temperature is below the combustion temperature but the combustion rate might be nonzero, such as in instants or locations in which there is a positive temperature fluctuation reaching above the mean temperature. To this effect, positive temperature fluctuations are associated with positive fluctuations in the reaction rate and contribute to the increase in the variance of dry temperature, $\overline{T'_d T'_d}$. Similarly, when the mean temperature is greater than the minimum combustion temperature (i.e., the reaction is occurring in more than half the available fuel), negative temperature fluctuations (or cooler temperatures in the distribution) can represent locations and instances at which the localized temperature is not sufficient to support the reaction, i.e., it is too cold to react. Thus, there is a negative fluctuation in the reaction rate. However, there are other contributions to the variations in reactions, such as localized mixing and oxygen concentrations, with increasing fraction of the volume above the critical temperature. Although the correlation, $\overline{T'_d F'_f}$, is expected to be positive, it will decrease with decreasing fraction of the temperature distribution above the critical temperature. This is conceptually shown in Fig. 2. Here, we expect the correlation to be closer to zero when $R_{combust}$, which is the fraction of dry fuel that is hot enough to react, is large. However, we anticipate the strongest correlation when less fuel is above the critical temperature ($R_{combust}$ is small). Considering this, we approximate the correlation as

$$\overline{T'_d F'_f} = c_{T_d F} \overline{F'_f} \sqrt{\overline{T'_d T'_d}} (1 - R_{combust}). \quad (32)$$

where $c_{T_d F}$ is taken to be 0.7. This constant must be empirically determined and here we estimate it to be 0.7 using the little fire data we have available. However, we will return to this constant in future studies.

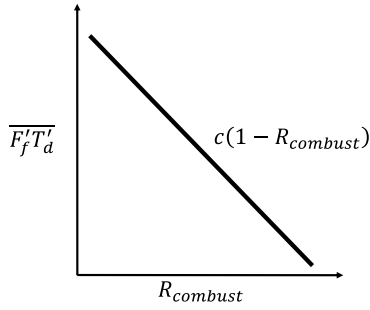


Fig. 2. Conceptual plot of the covariance of the reaction rate and dry temperature, $T'_d F'_f$, versus the fraction of dry fuel reacting, $R_{combust}$. c is a function of the temperature and the reaction rate.

The final unclosed term in Eq. (30), $\overline{T'_d T'_g}$, is the correlation between fluctuations in dry fuel temperature and gas temperatures. The correlation between these temperatures are largely related to the rate of convective heat transfer, which lower the temperature difference between adjacent gases and solids. When the convective heat transfer rate is high, perturbations in dry solid temperature are strongly related to the gas temperature perturbations. Since $\overline{T'_d T'_g}$ is symmetric in T'_d and T'_g , so should be the modeled term. This covariance is expected to increase depending on the magnitude of the variance of both the dry fuel and gas temperature (due to its symmetry), as well as the strength of the convective heat transfer. As the convective heat transfer coefficient increases, there will be greater energy transfer between the gas and solid phases and thus a stronger correlation between the fluctuations. To this end, we propose the following expression for the dry fuel and gas temperature covariance:

$$\overline{h a_{v,d}} \left(\overline{T'_d T'_g} \right) = \overline{h a_{v,d}} \left(1 - e^{-c_h \frac{\bar{h}}{h_{norm}}} \right) \left(\frac{\overline{T'_g T'_g} + \overline{T'_d T'_d}}{2} \right). \quad (33)$$

In this equation, h_{norm} is the normalization constant for the convective heat transfer coefficient, which is the approximate background value before ignition or heating. In the current study, h_{norm} is assigned the value of $25.0 \text{ W m}^{-2} \text{ K}^{-1}$ which is representative of the ambient value of h in FIRETEC before fire and during low wind conditions, and $c_h = 5$. The constant, c_h was determined by comparing modeled fire behavior over a variety of values ranging from 1 to 5 (not shown) for simple scenarios. This constant must be determined using empirical methods and we estimate it using the little fire data we have available. However, we will return to this (and other constants) in future work.

We now apply the same decomposition and derivation to the instantaneous wet solid temperature equation (Eq. (12)). Thus, taking the ensemble average of the expression yields:

$$\begin{aligned} c_{p,sw} \left(\overline{\rho_{sw} T'_w \frac{\partial T'_w}{\partial t}} + \overline{T'_w \rho'_{sw} \frac{\partial T'_w}{\partial t}} + \overline{T'_w \rho'_{sw} \frac{\partial T'_w}{\partial t}} \right) \\ = \overline{T'_w q'_w} + \overline{h a_{v,sw}} \left(\overline{T'_w T'_g} - \overline{T'_w T'_w} \right) \\ + \overline{h} \left(\overline{T'_w a'_{v,sw} T'_g} + \overline{T'_w a'_{v,sw} T'_g} \right) \\ - \overline{h} \left(\overline{T'_w a'_{v,sw} T'_w} + \overline{T'_w a'_{v,sw} T'_w} \right) \\ + \overline{a_{v,sw}} \left(\overline{T'_w h' T'_g} + \overline{T'_w h' T'_g} \right) \\ - \overline{a_{v,sw}} \left(\overline{T'_w h' T'_w} + \overline{T'_w h' T'_w} \right) \\ + \overline{a'_{v,sw} h' T'_w} \left(\overline{T'_g} - \overline{T'_w} \right) \\ + \overline{T'_w h' a'_{v,sw} T'_g} - \overline{T'_w h' a'_{v,sw} T'_w} \\ + \overline{F'_f T'_w H_f \Theta_w} - \overline{F'_{H_2O} T'_w H_{H_2O}}. \end{aligned} \quad (34)$$

Now, applying analogous simplifications that were discussed previously for the dry fuel equation returns:

$$\frac{\partial \overline{T'_w T'_w}}{\partial t} = \frac{2}{c_{p,sw} \rho_{sw}} \left[\overline{T'_w q'_w} + \overline{h a_{v,w}} \left(\overline{T'_w T'_g} - \overline{T'_w T'_w} \right) + \overline{F'_f T'_w H_f \Theta_w} - \overline{F'_{H_2O} T'_w H_{H_2O}} \right]. \quad (35)$$

Since we assume that the fraction of energy from the combustion process deposited on the wet fuel, Θ_w , is negligible, $F'_f T'_w H_f \Theta_w$ will have no contribution. Combustion is not occurring in the wet fuels and so the local retention of heat at the site of the reaction is not on the wet fuels. Thus there should be little to no energy from the combustion process directly contributing to wet fuel temperature changes. This assumption does not preclude the reaction from heating the wet fuels. In this proposed version, the reactions can heat the wet fuels because elevated-temperature dry fuels heat the gases and the gases convectively heat the wet fuels. Ultimately, when this model is fully implemented in FIRETEC, the wet fuels will also be heated by the dry fuels directly via radiation heat transfer but this mechanism is not in the current formulation. Thus, the only term left to complete the closure is the covariance of wet fuel temperature and evaporation rate, $\overline{F'_{H_2O} T'_w}$. Using the radiation and convection heat transfer rates, we can formulate the rate at which energy is added to the wet material. When the energy gained by the wet fuels causes the upper limit of the wet fuel distribution to reach or exceed the vaporization temperature (without enforcing the phase change on water or removing the energy of vaporization), evaporation of water begins. The energy available to evaporate water, $\overline{E_w}$, is related to the evaporation rate by $\overline{F_{H_2O}} = \overline{E_w} / H_{H_2O}$. We define a theoretical ratio for the fraction of wet fuel mass, R_{H_2O} , which would have risen above the evaporation temperature if evaporation had not commenced, assuming the distribution of temperature is symmetric about the mean (for simplicity). Thus, we have:

$$R_{H_2O} = \frac{T_{w,max} - T_{vap}}{2 C_{pdf} \sqrt{T'_w T'_w}}, \quad (36)$$

where C_{pdf} is a constant with a value as the ratio of halfwidth of the temperature distribution to the standard deviation and $T_{w,max}$ is the maximum temperature in the cell. Moreover, this constant depends on the type of distribution that would be assumed. The mean evaporation rate is therefore determined to be:

$$\frac{\int_{T_{w,min}}^{T_{w,max}} F_{H_2O}(T) dT}{\int_{T_{w,min}}^{T_{w,max}} dT} = \overline{F_{H_2O}}. \quad (37)$$

Here, $F_{H_2O}(T)$ is the evaporation rate associated with fuel at any specific temperature, T and $T_{w,min}$ is the minimum temperature in the cell. Now, we define a normalized evaporation rate, F^* as:

$$F^*_{H_2O} = \frac{F_{H_2O}(T)}{\overline{F_{H_2O}}}, \quad (38)$$

where

$$F^*_{H_2O} = \begin{cases} 0, & T_{w,min} < T < T_{vap} \\ \frac{1}{R_{H_2O}}, & T_{vap} \leq T < T_{w,max} \end{cases}. \quad (39)$$

This yields unity for the mean normalized vaporization rate:

$$\overline{F^*_{H_2O}} = \frac{\int_{T_{w,min}}^{T_{w,max}} F^* dT}{\int_{T_{w,min}}^{T_{w,max}} dT} = \frac{\int_{T_{vap}}^{T_{w,max}} \frac{1}{R_{H_2O}} dT}{2 C_{pdf} \sqrt{T'_w T'_w}} = 1. \quad (40)$$

Decomposing $F^*_{H_2O}$ into its mean and fluctuating components reveals:

$$F^*_{H_2O} = \overline{F^*_{H_2O}} + F'^*_{H_2O} = 1 + F'^*_{H_2O}. \quad (41)$$

Using these definitions we can compute $\overline{F'_{H_2O} T'_w}$ as:

$$\overline{F'_{H_2O} T'_w} = \overline{F_{H_2O}} \frac{\int_{T_{wmin}}^{T_{wmax}} F_{H_2O}^* T'_w dT}{\int_{T_{wmin}}^{T_{wmax}} dT} = \overline{F_{H_2O}} \frac{\int_{T_{wmin}}^{T_{wmax}} (F_{H_2O}^* - 1) T'_w dT}{2C_{pdf} \sqrt{\overline{T'_w T'_w}}} \quad (42)$$

where the temperature range of the wet solid is

$$\overline{T_w} - C_{pdf} \sqrt{\overline{T'_w T'_w}} \leq T_w \leq \overline{T_w} + C_{pdf} \sqrt{\overline{T'_w T'_w}}. \quad (43)$$

Given the definition of $F_{H_2O}^*$, this simplifies to

$$\overline{F'_{H_2O} T'_w} = \overline{F_{H_2O}} \frac{\int_{T_{vap}-\overline{T_w}}^{C_{pdf} \sqrt{\overline{T'_w T'_w}}} \left(\frac{1}{R_{H_2O}} - 1 \right) T'_w dT'}{2C_{pdf} \sqrt{\overline{T'_w T'_w}}}. \quad (44)$$

Using Eq. (36) in the lower limit of the integral we arrive at:

$$\begin{aligned} \overline{F'_{H_2O} T'_w} &= \overline{F_{H_2O}} \left(\frac{1}{R_{H_2O}} - 1 \right) \\ &\times \frac{\left(C_{pdf} \sqrt{\overline{T'_w T'_w}} \right)^2 - \left(C_{pdf} \sqrt{\overline{T'_w T'_w}} - 2R_{H_2O} C_{pdf} \sqrt{\overline{T'_w T'_w}} \right)^2}{4C_{pdf} \sqrt{\overline{T'_w T'_w}}} \end{aligned} \quad (45)$$

Manipulating and rearranging these terms, we arrive at:

$$\overline{F'_{H_2O} T'_w} = \overline{F_{H_2O}} C_{pdf} \sqrt{\overline{T'_w T'_w}} (1 - R_{H_2O})^2. \quad (46)$$

2.4. Final equations

The following subsection presents a summary of the new model equations with the closure completed for all terms.

$$\begin{aligned} \frac{\partial \overline{T_d}}{\partial t} &= \frac{1}{c_{pf} \rho_d} \left[\overline{q_d} + \overline{h a_{v,d}} (\overline{T_g} - \overline{T_d}) + \frac{\partial h}{\partial T_g} \overline{T'_g T'_g a_{v,d}} + \overline{F_f H_f \Theta_d} \right. \\ &\quad \left. + \overline{F_{H_2O}} \frac{c_{pf}}{r_{moist,w}} (\overline{T_{vap}} - \overline{T_d}) - \overline{F_{H_2O}} \frac{c_{pf}}{r_{moist,w}} \sqrt{\overline{T'_d T'_d}} \frac{\overline{T_d} - \overline{T_{vap}}}{\overline{T_d}} \right] \end{aligned} \quad (47)$$

$$\frac{\partial \overline{T_w}}{\partial t} = \frac{1}{c_{psw} \rho_{sw}} \left[\overline{q_w} + \overline{h a_{v,sw}} (\overline{T_g} - \overline{T_w}) + \frac{\partial h}{\partial T_g} \overline{T'_g T'_g a_{v,sw}} - \overline{F_{H_2O}} H_{H_2O} \right] \quad (48)$$

$$\begin{aligned} \frac{\partial \overline{T'_d T'_d}}{\partial t} &= \frac{2}{c_{pf} \rho_d} \left[-4 \overline{a_{v,d}} \epsilon \sigma \gamma \overline{T_d}^3 \overline{T'_d T'_d} \right. \\ &\quad \left. + \overline{h a_{v,d}} \left(\frac{\overline{T'_g T'_g} + \overline{T'_d T'_d}}{2} \left(1 - e^{-c_h \frac{\overline{h}}{h_{norm}}} \right) - \overline{T'_d T'_d} \right) \right. \\ &\quad \left. + c_{T_d F} \overline{F_f} \sqrt{\overline{T'_d T'_d}} (1 - R_{combust}) (H_f \Theta_d) - \overline{F_{H_2O}} \frac{c_{pf}}{r_{moist,w}} \overline{T'_d T'_d} \right. \\ &\quad \left. - \overline{F_{H_2O}} \frac{\sqrt{\overline{T'_d T'_d}}}{\overline{T_d}} (\overline{T_d} - \overline{T_{vap}})^2 \frac{c_{pf}}{r_{moist,w}} \right] \end{aligned} \quad (49)$$

and

$$\begin{aligned} \frac{\partial \overline{T'_w T'_w}}{\partial t} &= \frac{2}{c_{psw} \rho_{sw}} \left[-4 \overline{a_{v,sw}} \epsilon \sigma \gamma \overline{T_w}^3 \overline{T'_w T'_w} \right. \\ &\quad \left. + \overline{h a_{v,sw}} \left(\frac{\overline{T'_g T'_g} + \overline{T'_w T'_w}}{2} \left(1 - e^{-c_h \frac{\overline{h}}{h_{norm}}} \right) - \overline{T'_w T'_w} \right) \right. \\ &\quad \left. - \overline{F_{H_2O}} C_{pdf} \sqrt{\overline{T'_w T'_w}} (1 - R_{H_2O})^2 H_{H_2O} \right] \end{aligned} \quad (50)$$

where $\frac{\partial h}{\partial T_g}$ is described in Eq. (27).

3. Proof of concept simulations

The new approach described here is intended to capture sub-grid variability in temperatures, and thus increase the generality of wildland fire simulation capabilities. This enables properly simulating high- and low-intensity fires. This formulation constitutes the first stage in the development of a multi-phase coupled fire/atmosphere model, which has so far been confined to the solid phase. Since solids are not moving (no advection or spatial diffusion terms), we can study the performance in a single $1 \text{ m} \times 1 \text{ m} \times 1 \text{ m}$ control volume where the externally-driven conditions are prescribed, e.g. wind speed, upstream gas temperature, upstream oxygen concentration, and initial fuel moisture. In order to understand the performance of the proposed models (Eqs. (47)–(50)), we developed a series of idealized tests by varying initial fuel moisture conditions, wind speeds and upstream gas temperatures. The wet fuels (fuels at their initial moisture state) are assigned an initial bulk density of 0.5 kg m^{-3} and moisture fractions of (a) 0.05; (b) 1; and (c) 2. These correspond to fuel conditions similar to (a) dry dead needles and fine brachwood or matted dead grass; (b) live conifer fine branchwood and needles; and (c) live deciduous fine branchwood and leaves, respectively. Wind speeds have constant values of 0.1 m s^{-1} , 1 m s^{-1} and 2 m s^{-1} as this is a plausible set of wind speeds very near the ground (height below 1 m) in the vicinity of a surface fire. For a special case, we apply a wind speed value of 4 m s^{-1} , which constitutes a high-intensity fire. In these proof-of-concept simulations, we aim to explore a range of plausible scenarios by varying some of the primary driving factors for fire: wind, moisture and upwind temperatures. These factors are important for determining fire intensity and spread. For the purpose of this paper, we define the range of wildfire intensity as low-intensity fires that have depths and flame lengths 10s of centimeters, up to intense fires that have burning zones of 10s of meters and flame lengths of similar size.

Even though the focus of these proof-of-concept simulations is modeling the solid phase temperatures and their variations, it is necessary to vary the local gas temperature for the closure of the convective heat transfer terms. For this purpose, a simplified evolution equation is developed that combines the prescribed velocity and upwind temperature, the convective heat transfer coefficient, an area per unit volume, and a grossly simplified radiation energy sink. This expression estimates the gas temperature in the control volume:

$$\begin{aligned} c_{v,air} \rho_g \frac{\partial \overline{T_g}}{\partial t} &= \overline{q_g} - c_{v,air} \rho_g U \frac{\partial \overline{T_g}}{\partial x} \\ &\quad + \overline{h a_{v,d}} (\overline{T_d} - \overline{T_g}) + \overline{h a_{v,sw}} (\overline{T_w} - \overline{T_g}) + \overline{F_f H_f \Theta_g} \end{aligned} \quad (51)$$

Here, $c_{v,air}$ is $718 \text{ J kg}^{-1} \text{ K}^{-1}$, $q_g = -\frac{O_{2,ambient} - O_2}{O_{2,ambient}} \sigma \overline{T_g}^4$, which is the radiation loss scaled by the oxygen depletion that relates gas emissivity to combustion products in an oxygen poor environment, x is the spatial coordinate, and Θ_g is 0.75 (75% of reaction energy deposited in gas and 25% in the solid), which is the fraction of reaction energy absorbed by the gas phase. These values are within range with those observed in FIRETEC, and we do not allow them to vary for simplicity. This equation for the gas temperature is simply intended to capture the fact that there is feedback between the solid and gas temperatures and the influences of energy in surrounding regions on gas temperatures.

The variance of gas temperatures is prescribed based on the mean gas temperature using the following equations. This first equation,

$$\overline{T'_g T'_g} = \left(30 + \frac{\overline{T_g} - 243.59}{3} \right)^2 \quad (52)$$

is the variance assigned to the low-intensity gas scenario, which ensures that the minimum gas temperature in the assumed wide distribution does not fall below 300 K . The second version of the prescribed gas variance is:

$$\overline{T'_g T'_g} = \left(60 + \frac{\overline{T_g} - 300}{6} \right)^2 \quad (53)$$

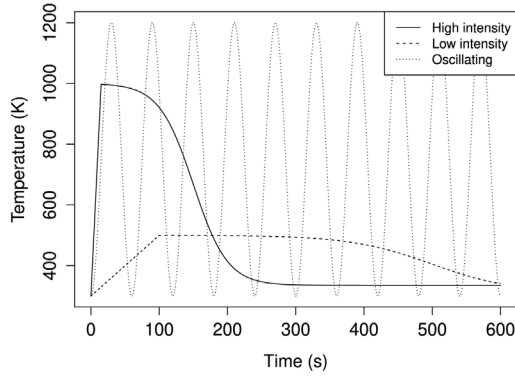


Fig. 3. Prescribed upwind gas temperature over time for the high-intensity, low-intensity and oscillating scenarios.

which we assigned for the other simulations. In subsequent phases of this study, related to the development of a multi-phase sub-grid fire-atmosphere model, these gas temperature equations are replaced with full transport equations, similar to the technique applied for the solid phase in the current study.

Initially, the gas temperatures in the control volume in all of the idealized simulation were assumed to be 300 K, before upwind gases began to advect into the control volume. High-intensity fire scenarios were simulated by assigning an upwind mean gas temperature that starts at 300 K, and ramps up to 1000 K over 15 s and tapers off following this relation:

$$\overline{T}_{g_{uw}} = 300 + \frac{700}{2} \left(0.95 - 0.95 \tanh \left(\frac{t - 15}{50} \right) + 0.05 \right), \quad (54)$$

and the low-intensity fires were simulated with the upwind temperatures rising from 300 K to 500 K over 100 s and tapers off as:

$$\overline{T}_{g_{uw}} = 300 + \frac{200}{2} \left(0.95 - 0.95 \tanh \left(\frac{t - 500}{120} \right) + 0.05 \right). \quad (55)$$

Additionally, we prescribe an oscillating upwind gas temperature with the following equation:

$$\overline{T}_{g_{uw}} = 750 + 450 \sin \left(\frac{(t - 15)2\pi}{60} \right). \quad (56)$$

All three upwind mean gas temperature prescriptions for the idealized scenarios are plotted in Fig. 3.

The first two temperature scenarios, involving near-sustained elevated gas temperatures, were designed to reduce the complexity of environmental drivers with the elevated temperature that represent gases advected from upwind with the approaching fire. The third gas temperature paradigm was chosen specifically to highlight the response of the model in dynamic environments with oscillating conditions. High-intensity fire scenarios are unlikely to coincide with light winds and thus we used only the case of wind speed at 4 m s^{-1} and temperature of 1000 K. Gas temperatures at or exceeding 1000 K are frequently observed in high-intensity crown fire (e.g. Taylor et al., 2004). The time step for all simulations is 0.001 s and we temporally discretize the differential equations using an explicit forward-in-time Euler method. The simulations ran for at least 600 s.

The size scale of the fuel (half of the volume to surface area ratio) remains constant and is prescribed as 0.0006 m, which corresponds to roughly that of thermally thin grass, needles, or fine branchwood. Thermally thin fuel refers to fine fuel particles that have no internal temperature gradients. As such, an individual fuel particle will warm and cool uniformly. Non-thermally thin fuel particles will be addressed in future efforts, which would build on some approaches that have been outlined in this document.

Sub-grid turbulent kinetic energy (TKE) is fixed at $k_a = 0.125U^2$, $k_b = 0.005U^2$ and $k_c = 0.2k_b \text{ m}^2 \text{ s}^{-2}$, where U is the prescribed scalar

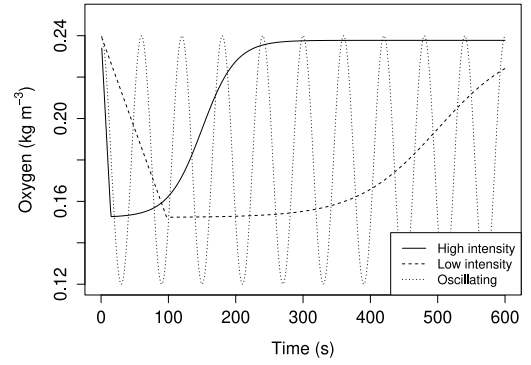


Fig. 4. Upwind oxygen concentrations where changes are inversely proportional to temperature changes.

wind speed. FIRETEC incorporates three sub-grid TKE scales (and their associated turbulence energy spectra) corresponding roughly to the unresolved scales associated with vegetation structure. Additional information on sub-grid TKE in FIRETEC is discussed by Linn (1997). For the purposes of this concept demonstration, the turbulent length scales are equivalent to the distance between larger vegetation structures (e.g. shrubs), branches, and needles.

The radiation loss terms are computed using the mean and variance of the wet and dry fuel temperatures to compute T^4 and blackbody radiation. The effective area that radiates energy away from the solid is estimated based on the surface area per unit volume times γ , which is the ratio of the fuel depth height to cell height (a compression factor):

$$q = \gamma a_v \epsilon \sigma T^4. \quad (57)$$

While radiation ahead of the flame front has a role in preheating fuels, radiation alone does not typically induce fire spread in fine wildland fuels that are loosely packed due to attenuation in low-density discontinuous fuels and the fact that convective cooling between fine fuel elements counteracts radiative heating, as was discussed by Finney et al. (2015). Results from their experiments provide strong evidence that convection is largely responsible for wildland fire spread (Cohen and Finney, 2022a,b). Thus in the interest of simplicity, we omit the influences of radiative heating in this initial testing phase. The radiative heating will be addressed in more detail in subsequent efforts.

The evaporation rate is calculated by first determining the difference between the energy gained by the wet fuel through convective and radiative heat transfer within one time step and the energy that it takes to raise the temperature distribution to the point where the max temperature reaches 373 K. This residual energy is the energy available to evaporate water within the time step and determine the water evaporation rate. The theoretical maximum temperature, $T_{w_{max}}^*$, that would be reached within a time step without accounting for the phase change provides an estimate for the fraction of fuel, R_{H_2O} , that would be above 373 K due to the radiative and convective heating and cooling. For this initial effort, we use a top hat distribution. Using this simplified distribution, $C_{pdf} = \sqrt{3}$ in Eq. (36). We recognize that if a normal distribution is applied instead, R_{H_2O} is a form of the error function (or cumulative distribution function for a Gaussian shape). More details on the error function can be found in Jeffrey (1995) and we will be exploring this topic in the future, separately.

We apply a similar philosophy to determine what fraction of the fuel in a cell is above the critical temperature for combustion, ψ . This fraction is used in the mixing limited reaction rate as described by Linn (1997).

A simplified model for the advection and consumption of oxygen density is used to represent the depletion and replenishment of oxygen with time. The available oxygen is initialized as 21% of the air density,

0.21 ρ_{ambient} , and over time it is calculated explicitly using the following equation:

$$\frac{\partial O_2}{\partial t} = -F_f N_{\text{oxygen}} - U \frac{\partial O_2}{\partial x}. \quad (58)$$

Here, N_{oxygen} is the stoichiometric coefficient for oxygen in the combustion reaction (Drysdale, 1985) normalized by the total mass of reactants. The upwind oxygen value is related to the upwind temperature, such that as temperature decreases/increases oxygen increases/decreases proportionally. Corresponding to the upwind drop in temperature, we assign upwind oxygen, such that:

$$\overline{O_{2_{\text{up}}}} = 0.15 + \frac{0.09}{2} \left(0.95 - 0.95 \tanh \left(-\frac{t-15}{50} \right) + 0.05 \right) \quad (59)$$

in the high-intensity simulations, and

$$\overline{O_{2_{\text{up}}}} = 0.15 + \frac{0.09}{2} \left(0.95 - 0.95 \tanh \left(-\frac{t-500}{120} \right) + 0.05 \right) \quad (60)$$

for the low-intensity cases. Lastly, the upwind oxygen concentration in the oscillating simulations is

$$\overline{O_{2_{\text{up}}}} = 0.18 - 0.06 \sin \left(\frac{(t-15)2\pi}{60} \right). \quad (61)$$

All three scenarios are plotted in Fig. 4.

Finally, we only apply the equations for temperature of the wet/dry fuel equations and their variances when their respective density is greater than $1 \times 10^{-6} \text{ kg m}^{-3}$.

4. Results and discussion

4.1. Proof-of-concept simulation results

We begin with scenarios of high-intensity fire placed upwind of the control volume. We simulate high upwind temperature with high wind speed for all local moisture scenarios shown in Fig. 5 and Table 1. In these simulations, the mean upwind gas temperature is raised from 300 K to 1000 K over 15 s with a slow decline back to ambient temperature. It is unlikely that a 1000 K gas temperature would coincide with light winds. Thus for this high-intensity simulation, we present the results for only the case of 4 m s^{-1} wind speed, applied to all three fuel moisture scenarios (5%, 100% and 200%).

In Fig. 5, mean wet and dry fuel temperatures are only shown in cases with the density above $1 \times 10^{-6} \text{ kg m}^{-3}$. The blue solid line with circles indicates the mean wet fuel temperature, the red line with squares is the mean dry fuel temperature, the light gray line is mean gas temperature, the solid purple line is the upwind prescribed gas temperature, and the dashed blue and dotted red lines are the wet fuel and dry fuel density, respectively. Shading corresponds to one standard deviation above and below the mean temperature value.

In all moisture fraction scenarios, a fraction of wet fuel is quickly dried and dry fuel begins to burn within the first 13 s of all simulations. It should be noted that there is an assumption that there are burning ashes etc. present, such that ignition is piloted. At the onset of combustion in the fuel with a moisture fraction of 0.05, 99% of the fuel is already dried (i.e., 99% moved from the wet to dry fuel category) and thus available for consumption. This can be contrasted to 33% and 17% of the fuels that have been dried when combustion starts for the fuels with moisture fractions 1 and 2, respectively as shown in Table 1. The maximum temperature is slightly higher in the lower moisture fraction scenarios, but the time for the peak temperature differs only by 6 s among these three simulations. The similarity between these three cases is indicative of the fact that the strong winds and high temperatures are very significant and they overwhelm the effects of moisture on combustion initiation. It is important to remember that the prescribed high-intensity conditions are associated with fire upwind of the control volume, likely indicating an abundance of dry fuel in that region. The similarity of the results relates to the fact that when a fire moves from one set of conditions to a new set of conditions,

Table 1

1000 K gas temperature simulation results under wind [U (m s^{-1})], and moisture fraction [$r_{\text{moist},\text{up}}$] scenarios for evaporation initiation time [t_{e_0} (s)], evaporation completion [t_{e_f} (s)], combustion initiation [t_{c_0} (s)], density of dry fuel at combustion initiation [ρ_{d_c} (kg m^{-3})], the peak temperature [T_{max} (K)], the time of peak temperature [$t_{T_{\text{max}}}$ (s)], the time for 50% [$t_{f_{50}}$ (s)] and 75% [$t_{f_{75}}$ (s)] fuel consumption, and the density at 600 s [$\rho_{d_{600}}$ (kg m^{-3})].

U	$r_{\text{moist},\text{up}}$	t_{e_0}	t_{e_f}	t_{c_0}	ρ_{d_c}	T_{max}	$t_{T_{\text{max}}}$	$t_{f_{50}}$	$t_{f_{75}}$	$\rho_{d_{600}}$
4.0	0.05	1.8	10	9	0.495	1221	11	15	23	0.004
4.0	1.00	3.2	72	12	0.164	1087	15	21	28	0.004
4.0	2.00	4.3	508	13	0.085	1073	17	24	33	0.005

Table 2

500 K gas temperature for each wind and moisture scenario. The columns are the same as described in Table 1. The table is organized consecutively corresponding to Fig. 6 subfigures (a)–(i).

U	$r_{\text{moist},\text{up}}$	t_{e_0}	t_{e_f}	t_{c_0}	ρ_{d_c}	T_{max}	$t_{T_{\text{max}}}$	$t_{f_{50}}$	$t_{f_{75}}$	$\rho_{d_{600}}$
0.1	0.05	26	242	–	–	373	0	–	–	0.5
0.1	1.00	43	–	–	–	373	0	–	–	0.5
0.1	2.00	56	–	–	–	373	0	–	–	0.5
1.0	0.05	10	95	114	0.5	801	132	156	206	0.053
1.0	1.00	17	–	–	–	430	255	–	–	0.5
1.0	2.00	23	–	–	–	426	282	–	–	0.5
2.0	0.05	7	80	95	0.5	936	103	113	129	0.019
2.0	1.00	13	445	112	0.36	919	122	132	148	0.020
2.0	2.00	18	–	136	0.29	927	146	157	175	0.027

the changes to fire behavior do not occur instantaneously (time or space). Thus when our control volume has high moisture (i.e. moisture ratio, or fractions, of 1 or 2), the high-intensity fire from upstream still ignites the fuel and consumes it, but the energy release (proportional to the dry mass loss rate) is lower in the wetter fuel cases. We also note that the temperature begins to decrease after the initial reaction in all scenarios as a combined result of reduced oxygen availability leading to lower reaction rates and convective cooling. After 600 s, only 0.9% or less of the fuel remains in all simulations, which indicates near complete fuel consumption regardless of moisture content. This is consistent with observations and empirical models in high-intensity wildfire. During high-intensity crown fire, where observed in-fire mean gas temperatures exceed 1000 K (e.g. Taylor et al., 2004), the fraction of fine fuels (less than 5 mm diameter) that are consumed is high and often approaches 100% (Thompson et al., 2020; Forestry Canada Fire Danger Group, 1992; Call and Albini, 1997; Stocks et al., 2004; de Groot et al., 2022).

Reducing the upwind gas temperature and variance after 100 s provides enough time to examine the fire behavior simulated in the model at constant high-intensity. For all simulations presented here, it is important to remember that holding the wind and upwind gas temperature steady (and remaining steady for an extended period of time) is unrealistic, as any given location in a fire has a transient set of conditions as the fire approaches it and moves past. Thus we have chosen a simplified set of environmental conditions to expose the solid fuel to, but we recognize the importance of coupling this to the full set of dynamic conditions (which will be done as this solid model is connected to a similar gas model in the CFD context of FIRETEC) before the weight is put on the specifics of model results.

Evaluating the results in Fig. 6 and Table 2, we next examine the behavior of our proposed model for a lower-intensity upwind fire scenario and a lower-mean upwind gas temperature with a higher variance. These conditions are selected to illustrate the behavior of the proposed model during a low-intensity head fire impinging on a cell, or flanking/backing fire behavior where only a fraction of the gas temperature within the cell would be hot enough to initiate combustion in the dry fuel. In these scenarios, the upwind gas temperature begins at ambient, ramping up to 500 K over 100 s and slowly decreasing as shown in Figs. 3 and 6. The results presented in Figs. 6a–6c correspond

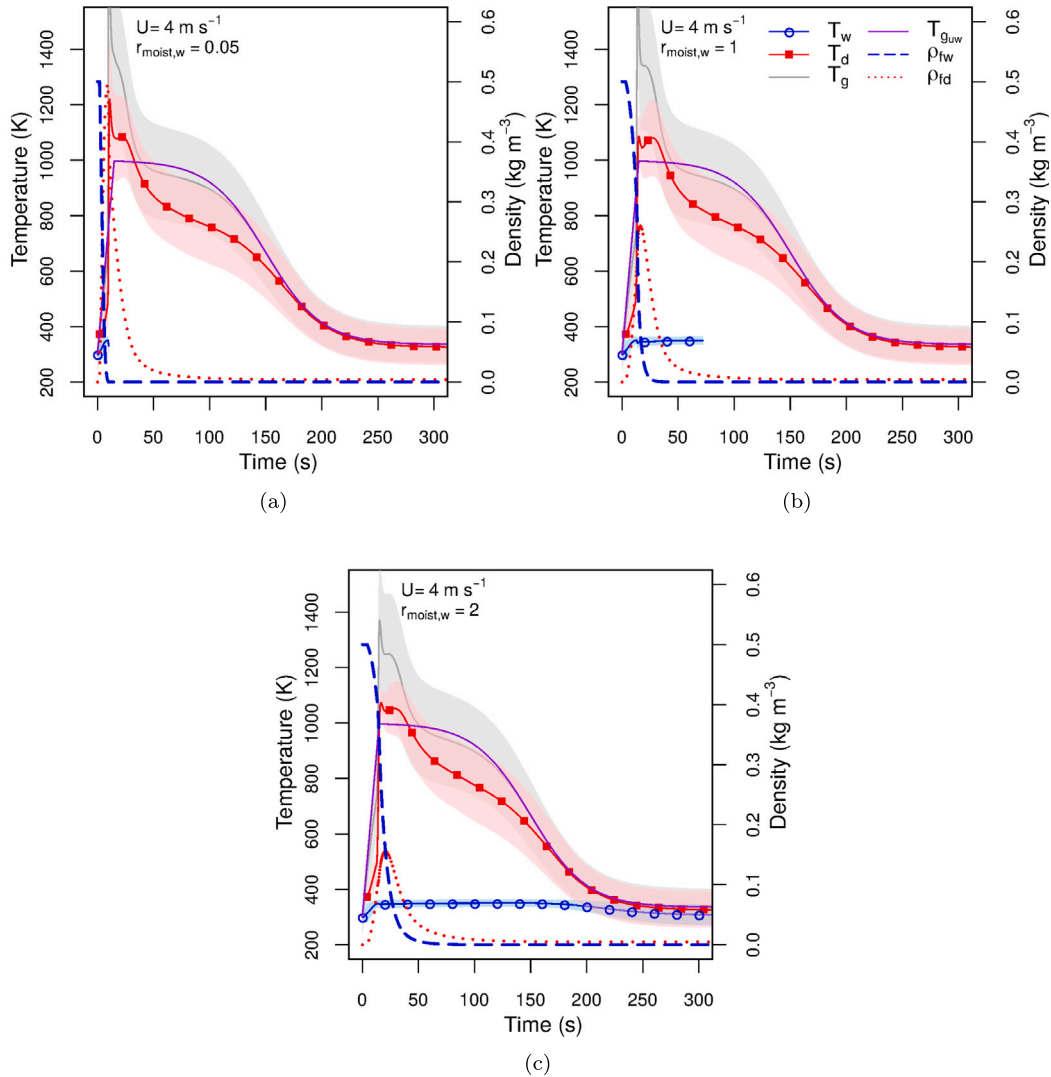


Fig. 5. Model results for high-intensity fire with 4 m s^{-1} winds at (a) moisture fraction 0.05, (b) moisture fraction 1 and (c) moisture fraction 2. Temperature is plotted only when the respective fuel density is above $1 \times 10^{-6} \text{ kg m}^{-3}$ and shading indicates 1 standard deviation above and below the mean temperatures.

to wind speed 0.1 m s^{-1} , Figs. 6d–6f to wind speed of 1.0 m s^{-1} , and Figs. 6g–6i to a wind speed of 2.0 m s^{-1} . Furthermore, Figs. 6a, 6d, and 6g correspond to moisture fraction of 0.05, Figs. 6b, 6e and 6h are moisture fraction of 1, and Figs. 6c, 6f and 6i show results for moisture fraction of 2.

In simulations where the wind speed is near calm (Figs. 6a–6c), convective heat transfer is not significant enough to warm the fuel and overcome radiative losses, which increase rapidly with temperature rise due to their dependence on the fourth power of temperature (we remind the reader that we are not simulating radiative gains and thus the primary source of energy before combustion is convection). Therefore no fraction of the fuel is warm enough to begin combustion in any of the scenarios. Increasing the wind speed to 1 m s^{-1} provides enough convective heating to induce combustion when the fuel is dry. However, the energy sink required to evaporate water from the fuel with a higher moisture content prevents combustion from occurring. Increasing the wind speed to 2 m s^{-1} results in all moisture scenarios reaching the threshold for combustion. Interestingly, the fuel consumption in all cases where combustion occurs is 89% or greater. This result is somewhat surprising since during a low-intensity burn we would expect less than 89% consumption. For these idealized cases with constant winds and steady gas temperature prescription, however,

we are not capturing the effects of cool air entrainment. This can contribute to residual unburned fuel. Furthermore, the elevated upwind temperatures persist for more than 5 min, which is likely unrealistic over a 1 m spatial scale in some of these scenarios. Arguably, a near-surface wind speed of 2 m s^{-1} would produce a higher intensity surface fire than we are prescribing upwind, especially for the driest fuel. For example, the Canadian Forest Fire Behavior Prediction system (Forestry Canada Fire Danger Group, 1992), an empirically-based system used by fire management agencies, predicts a moderately intense fire with 1.3 m s^{-1} forward rate of spread in dead matted grass that has a moisture content of 5% if we estimate the 10 m open wind speed to be 5.4 m s^{-1} using a simple logarithmic wind profile with 2 m s^{-1} wind at 1 m , roughness length $z = 0.05 \text{ m}$ and zero plane displacement $d = 0.65 \text{ m}$. Considering the depth of the fireline (being at most tens of meters deep) and the forward rate of spread, the residence time for such a fire would be much less than 5 min (Cheney and Sullivan, 2008; Wotton et al., 2012) in this case.

In simulations where wet fuel is still being converted to dry fuel during combustion (Figs. 6h and 6i), the initiation of burning coincides with a slight decrease in mean wet fuel temperature. Since the mass of wet fuel drops quickly in response to accelerated evaporation caused by the increase in gas temperature, the mean temperature of the wet

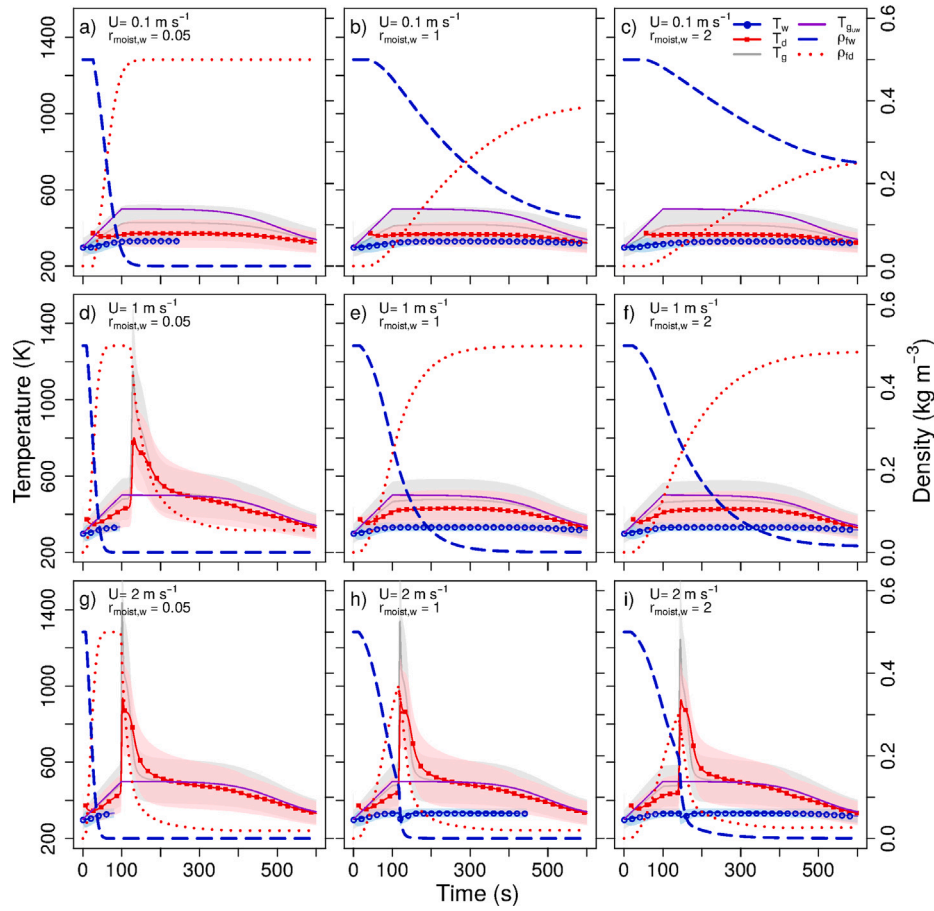


Fig. 6. Results for wind speed and moisture fractions applied to the low-intensity gas scenario.

Table 3

Terms and abbreviated symbols for Fig. 8.

Wet fuel terms contributing to the mean and variance of temperature			
α_w	\bar{q}_w	α_{uv}	$-4\bar{a}_{v,w} \epsilon \sigma \gamma \bar{T}_w^{-3} \bar{T}_w' \bar{T}_w'$
β_w	$\bar{h} \bar{a}_{v,w} (\bar{T}_g - \bar{T}_w)$	β_{uv}	$\bar{h} \bar{a}_{v,w} \left(\frac{\bar{T}_g' \bar{T}_g' + \bar{T}_w' \bar{T}_w'}{2} \left(1 - e^{-\frac{\bar{h}}{\bar{h}_{norm}}} \right) - \bar{T}_w' \bar{T}_w' \right)$
β_{w2}	$\bar{a}_{v,w} \frac{\partial \bar{h}}{\partial \bar{T}_g} \bar{T}_g' \bar{T}_g'$	β_{wv2}	–
δ_w	$-\bar{F}_{H_2O} H_{H_2O}$	δ_{wv}	$-\bar{F}_{H_2O} C_{pdf} \sqrt{\bar{T}_w' \bar{T}_w'} (1 - R_{H_2O})^2 H_{H_2O}$
ϵ_w	–	ϵ_{wv}	–
ϵ_{w2}	–	ϵ_{wv2}	–
Dry fuel terms contributing to the mean and variance of temperature			
α_d	\bar{q}_d	α_{dv}	$-4\bar{a}_{v,d} \epsilon \sigma \gamma \bar{T}_d^{-3} \bar{T}_d' \bar{T}_d'$
β_d	$\bar{h} \bar{a}_{v,d} (\bar{T}_g - \bar{T}_d)$	β_{dv}	$\bar{h} \bar{a}_{v,d} \left(\frac{(\bar{T}_g' \bar{T}_g' + \bar{T}_d' \bar{T}_d')}{2} \left(1 - e^{-\frac{\bar{h}}{\bar{h}_{norm}}} \right) - \bar{T}_d' \bar{T}_d' \right)$
β_{d2}	$\bar{a}_{v,d} \frac{\partial \bar{h}}{\partial \bar{T}_g} \bar{T}_g' \bar{T}_g'$	β_{dv2}	–
δ_d	$\bar{F}_f H_f \Theta_d$	δ_{dv}	$\bar{F}_f \sqrt{\bar{T}_d' \bar{T}_d'} (1 - R_{combust}) H_f \Theta_d$
ϵ_d	$\bar{F}_{H_2O} \frac{c_{pf}}{r_{moist,d,w}} (\bar{T}_{vap} - \bar{T}_d)$	ϵ_{dv}	$-\bar{F}_{H_2O} \frac{c_{pf}}{r_{moist,d,w}} \bar{T}_d' \bar{T}_d'$
ϵ_{d2}	$-\bar{F}_{H_2O} \frac{c_{pf}}{r_{moist,d,w}} \sqrt{\bar{T}_d' \bar{T}_d'} \frac{\bar{T}_d - \bar{T}_{vap}}{\bar{T}_d}$	ϵ_{dv2}	$-\bar{F}_{H_2O} \frac{\sqrt{\bar{T}_d' \bar{T}_d'}}{\bar{T}_d} (\bar{T}_d - \bar{T}_{vap})^2 \frac{c_{pf}}{r_{moist,d,w}}$

fuel will fall as the warmest of the wet fuel is converted to dry fuel and the cooler portions of the wet fuel remains. Furthermore, the sharp increase in temperature at the onset of combustion is more rapid than expected for a low-intensity scenario in a cell $1 \text{ m} \times 1 \text{ m}$ and is due to the fact that (1) we do not simulate cool air entrainment and temperature fluctuations from surrounding cells when the upwind gas is elevated, and (2) we may not be accurately capturing the oxygen

concentration in the control volume. This also likely contributes to a larger fraction of fuel being consumed than is expected during marginal conditions. These limitations will be corrected with the coupling of the gas equations to the fuel equations in the near future, where we capture the influence of adjacent cells (i.e., more realistic advection of gas and oxygen) and turbulent variations.

In Fig. 7, we show a comparison of results using an isolated cell from the current formulation of FIRETEC and the newly proposed method. The simulations presented in Fig. 7 are for the moderate wind speed and low-intensity scenarios shown in Fig. 6d–6f. It is important to note that the proposed method utilizes top hat distributions that shift and dilate based on the equations for the mean and the variance. The distribution for the original formulation is a fixed curve similar to a gaussian and thus the interpretation of the predicted distributions must be different. Both sets of simulations were driven by the same initial and boundary conditions as described in Section 3. Furthermore, both sets of equations are coupled to a gas equation and oxygen equation (Eqs. (51) and (58)). This comparison highlights differences between the current method in FIRETEC and the need for a scenario-dependent dynamic temperature distribution. While dry conditions result in combustion occurring in both the original and new formulations, when moisture content is high only the original formulation of the equations produces a combustion reaction. Furthermore, when conditions are driest, combustion occurs in less than half the time for the original formulation compared to the proposed formulation, which is a result of the fixed temperature distribution. This highlights the need for improved methods to capture the subgrid distributions of temperature and moisture, which are critical for spread and ignition in low-intensity scenarios. Combustion does not occur in either formulation when winds are near calm (not shown here for brevity).

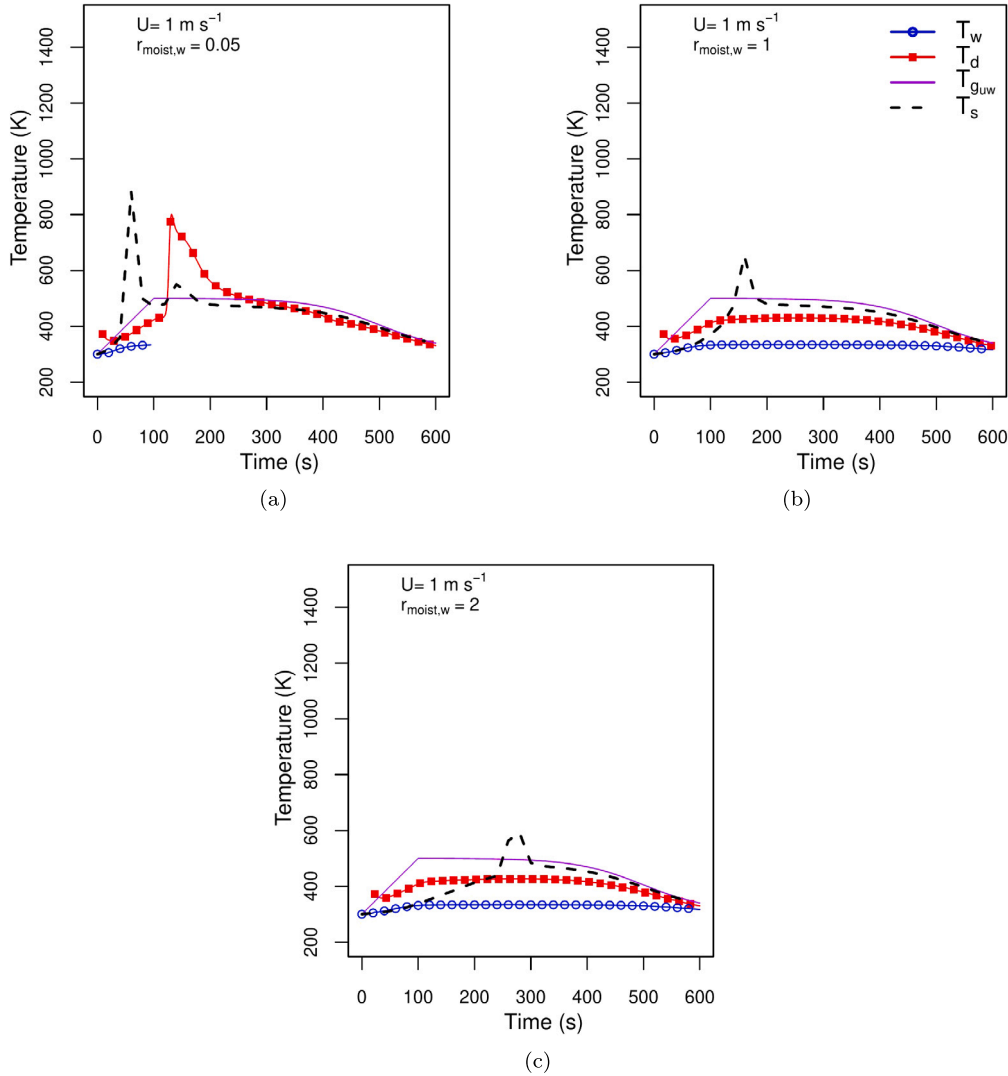


Fig. 7. Comparison of the current formulation in FIRETEC (dashed black lines) to the proposed formulation for low-intensity scenarios with moderate winds. Data for proposed simulations is the same as shown in Figs. 6(d)–6(f).

The main motivation behind this work is to improve the sub-grid models for fire behavior simulations through the development of new closure schemes. Thus, we proceed with examining the individual terms and closures in the proposed model, specifically looking at the processes in Fig. 6i. This simulation was selected since it highlights the most important processes in the lower intensity upwind scenarios, i.e., slower warming and evaporation, moderate wind speeds, higher moisture, and eventual but delayed combustion. Hereafter, we represent all terms in Fig. 8 related to radiation contribution as α_x , all terms related to convection as β_x , all terms related to the heat of combustion or heat of vaporization as δ_x , and all other terms as ϵ_x , where x denotes d for the mean dry fuel temperature, dv is the mean dry fuel temperature variance, w is the mean wet fuel temperature, and wv is the mean wet fuel temperature variance. In the case where β_x or ϵ_x have two terms, these terms are assigned in the order that they are shown in the governing equations that have been outlined in previous sections. These terms are more specifically outlined in Table 3.

Beginning with the solid wet fuel mean temperature and variance, as shown in Figs. 8a and 8b, the mean temperature rises and the variance increase in response to increasing gas temperature at the onset of the simulation. This is via convection before the onset of evaporation at 18 s. Once evaporation begins, convection source terms, β_w and β_{wv} ,

and the sinks associated with heat of evaporation, δ_w and δ_{wv} , increase the mean temperature and reduce the variance respectively, as warm wet fuel is being converted to dry fuel. Regarding the dry temperature results in Fig. 8c, the mean dry fuel temperature falls with the radiative and convective cooling sinks, α_d and β_d , which exceed the source of warm dry fuel, ϵ_d , until the gas temperature rises above the mean dry temperature. This results in positive convective heat transfer, which forces a rise in dry temperature. At the same time, we observe a rise in the variance (Fig. 8d) of the dry fuel, since the positive contribution from the convective term, β_{dv} , outweighs the sink from radiation, and the dry fuel mass source terms, α_{dv} and ϵ_{dv} , respectively (Fig. 8d).

The dry variance and mean temperature continue to rise until a fraction of mass in the dry fuel temperature distribution reaches 600 K (at approximately 136 s) and pyrolysis/combustion begins. The exothermic reaction source term, δ_d , quickly raises the mean temperature of the dry fuel. This is while the combined sources, δ_{dv} and β_{dv} , are greater than the combined sinks, α_{dv} , ϵ_{dv} and ϵ_{dv2} , resulting in a rapid net increase of the variance. As previously discussed for Figs. 6h and 6i, at the onset of combustion we observe energy and mass losses in the wet fuel, which are due to rapid heating. Thus, the sudden drop in δ_w results in a momentary decrease of the mean wet fuel temperature and an increase in the wet fuel variance as warm wet fuel is quickly converted to dry fuel.

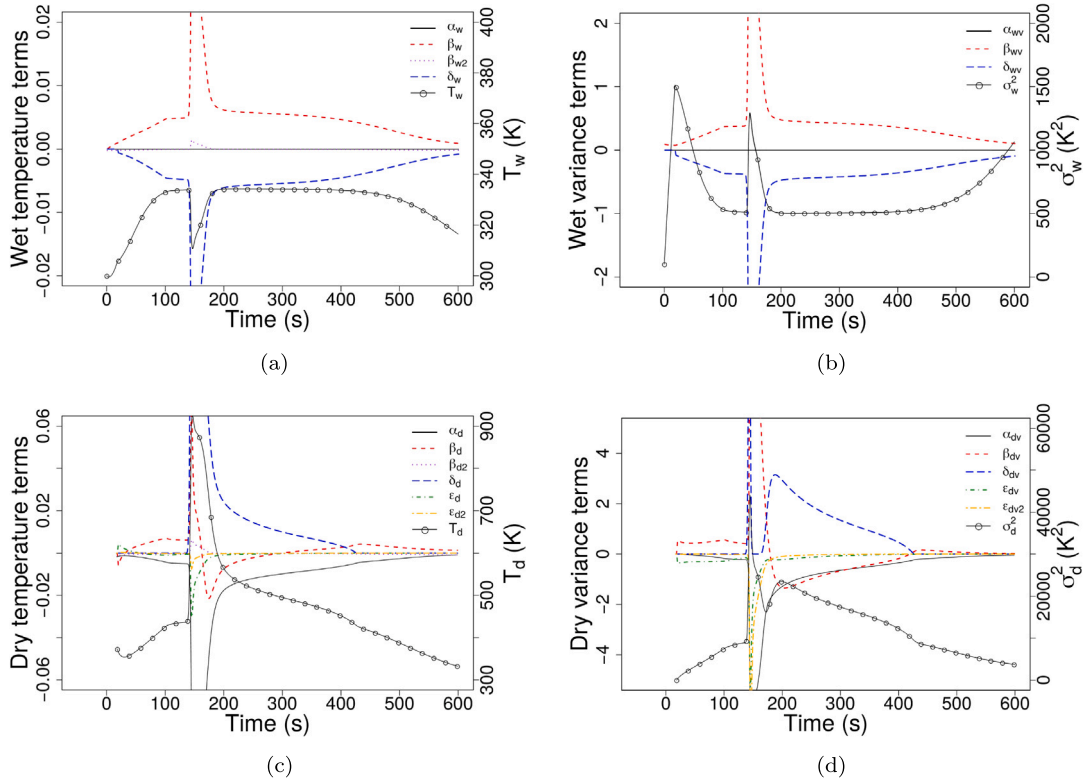


Fig. 8. Individual term contributions averaged over 1 s for (a) the wet fuel temperature equation, (b) the wet fuel variance equation, (c) the dry fuel temperature equation, and (d) the dry fuel variance equation in the wind 2 m s⁻¹, fuel moisture fraction 2 and gas temperature 500 K scenario. The terms in the legend appear as ordered in the derived equations and are discussed further in Table 3. All terms shown are multiplied by $\frac{dt}{c_p \rho}$ or $\frac{2dt}{c_p \rho}$ for the corresponding specific heat capacity and density.

The mass loss due to combustion coincides with depleted oxygen and lowering of the reaction rate, δ_d . This, combined with convective cooling and mass gain at lower temperatures (β_d and ϵ_d), leads to a drop in mean temperature shortly after combustion commences. Similarly, δ_{dv} in the variance equation falls as the reaction rate drops. This combined with the sinks related to radiation, α_{dv} , and cooling (convective, evaporative, and mass gain, β_{dv} , ϵ_{dv} , and ϵ_{dv2}) the variance falls as well. At this stage, the upwind prescribed gas temperature is decreasing and all source and sink terms are reduced in all equations until both the reaction and evaporation ceases and convection and radiation are the only contributing terms.

The qualitative examination of the individual terms in the reaction in the simulations with mean upwind gas temperatures ranging from 300 K to 500 K and a high variance provides a reasonable explanation for the observed fire behavior in the conceptual model presented here. Most of the known processes are represented in this simple scenario and the equations are stable and provide results consistent with expectations. Although we are unable to directly compare the results of this study with observed in-fire data to determine the accuracy of magnitude and relative contributions of the individual terms, the net fire behavior follows the expected trends. We acknowledge the scenarios presented are unrealistic given constant or steady wind, mean upwind gas temperatures and gas variance. However, we are able to examine the behavior of the model by removing the complexities of variations in gas temperature and wind speed due to turbulence. This also enables examining the impact of each of the terms and closures presented here.

The final set of idealized gas scenarios presented is driven by an oscillating upwind gas temperature, which alternates between 300 and 1200 K with a 60 s period as shown in Fig. 9 and Table 4. Wind and moisture are the same as outlined in Fig. 6. In nearly all simulations we observe a step-like structure in the density as a response to the fluctuations in gas temperature. As gas temperature increases, the

movement of mass from wet to dry accelerates, and the decrease in the rate of dry mass gains coincides with the slowing of the mass transfer. Moreover, this step-like structure is evident in the mass decrease of dry fuel as well, particularly in the two higher wind speed scenarios, in which convective heat transfer and mixing is stronger.

Combustion does not occur in the lowest wind speed simulations, even with maximum gas temperatures upwind reach 1200 K as there is not enough mixing. Furthermore, upwind gas temperatures only remain above 600 K for 36 s at a time before falling below 600 K in the oscillation. All scenarios where combustion occurs have near complete combustion (i.e., 2% or less fuel remains at the end of the simulation). This is not surprising as sufficient mixing and very hot gas temperatures contribute to the reaction consuming fine fuels quickly.

We observe a rapid rise in dry temperature at the onset of combustion in the higher wind speed simulations (Figs. 9d–9i), similar to the gas scenarios discussed earlier for Figs. 6 and 8. However in the moderate wind speed scenario with a slower fuel response time due to reduced convective heat transfer (Figs. 9d–9f), we observe a markedly cooler peak temperature with a slower decline when compared to the high-intensity scenarios (Table 1 and Fig. 5 where gas temperatures remain high. Because of this slower response time, when combustion finally occurs, the upwind temperature is already in the decreasing phase of the oscillation and so the control volume and upwind gas temperature is cooler at the onset of combustion. This leads to a slowed acceleration and deceleration of the reaction rate and a lower overall maximum temperature. This phase could loosely be compared to the effects of cool air advection from surrounding cells and turbulence- or vorticity-induced cooling. As discussed by Finney et al. (2015), local temperatures fluctuate rapidly as a result of the effects of turbulence and buoyancy-induced circulation, which can be periodic in both stream-wise and transverse directions. Since we are not incorporating these effects in the control volume boundary conditions, we can expect variation in reaction rate and mean dry fuel temperature

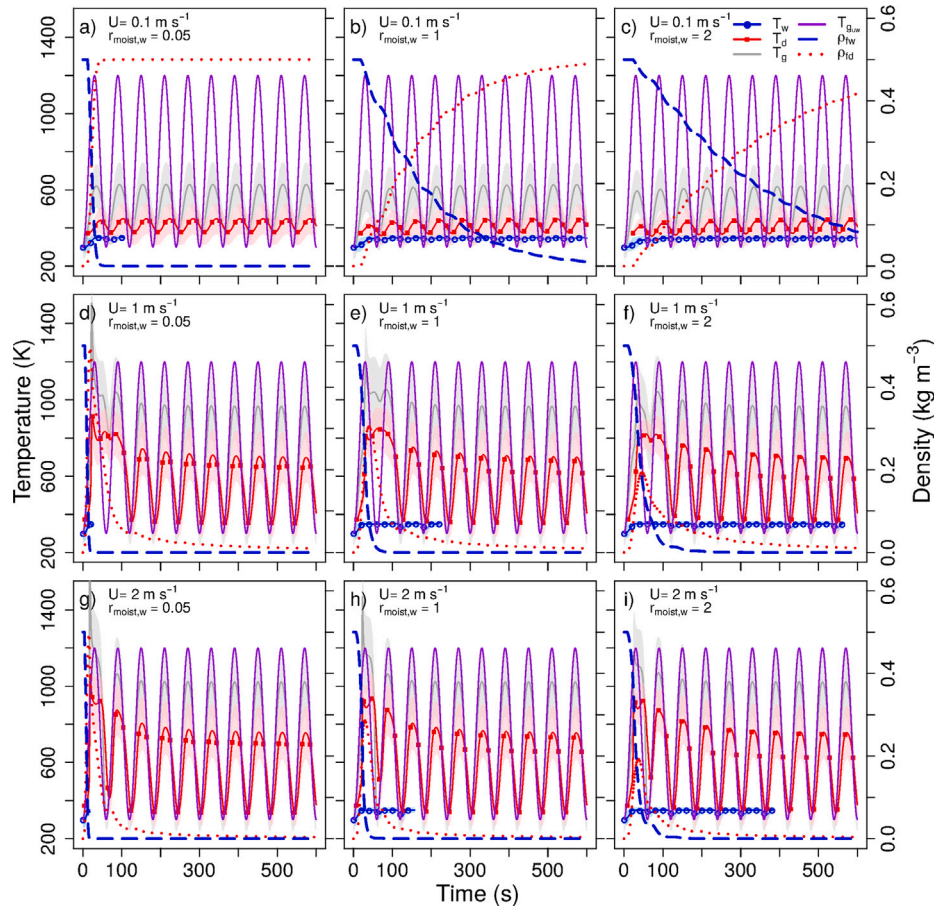


Fig. 9. Wind speed and fuel density scenarios for gas temperature oscillating between 1200 K and 300 K with a 60 s period. The wind and moisture scenarios are the same as described in Fig. 5.

Table 4

Oscillating gas temperature for each wind and moisture scenario. The columns are the same as described in Table 1.

U	$r_{moist,w}$	t_{e0}	t_{ef}	t_{c0}	ρ_{dc}	T_{max}	$t_{T_{max}}$	t_{f50}	t_{f75}	ρ_{d400}
0.1	0.05	12	104	–	–	448	163	–	–	0.5
0.1	1.00	18	–	–	–	447	584	–	–	0.5
0.1	2.00	23	–	–	–	444	584	–	–	0.5
1.0	0.05	5	23	19	0.496	915	25	49	69	0.009
1.0	1.00	8	220	25	0.169	850	63	56	76	0.010
1.0	2.00	11	561	26	0.089	821	56	63	93	0.011
2.0	0.05	4	18	16	0.496	1061	19	31	47	0.004
2.0	1.00	7	157	20	0.165	939	49	40	53	0.004
2.0	2.00	9	382	21	0.085	923	49	44	69	0.004

when coupling the unsteady gas equation and fuel equations in three-dimensional scenarios. Future work that includes more accurate oxygen advection should further improve the reaction and fuel consumption rates.

In these simulations, the lag and offset between the dry fuel temperature, the cell level gas temperature and the upwind gas temperature is most pronounced in the lower wind scenario for all three moisture fractions. This is due to the reduced convective energy transfer for solid-to-gas and gas-to-solid. The variations in wet fuel temperature in response to variation in gas temperature similarly increases with wind speed. Unlike the low-intensity scenario shown in Fig. 6, we observe a very modest decrease in wet fuel temperature during the onset of combustion. Instead, changes in wet fuel temperature are mainly a result of gas temperature variation in the control volume.

4.2. Effects of gas temperature variance on dry fuel

While we only present the results for a single control volume whose fuel evolution is not directly dependent of cell size (although the overly simplified gas temperature and oxygen equation assumes a 1 m upwind distance), the improvement of sub-grid temperature distribution relaxes the current restraint on cell size in three-dimensional formulations of FIRETEC. The proposed model for the evolution of sub-grid temperature distribution is expected to improve the current static shape of sub-grid temperature distribution in FIRETEC. While the cell size is not explicitly adjusted in the proposed model, we can instead achieve a similar result by prescribing a wide gas temperature distribution. This is because a fire approaching a larger cell will result in a wide range of sub-grid temperatures given a small fraction of fuel and gas in the large cell would initially warm while the remainder of the cell remains closer to the ambient temperature. In the next phases of this work, the inclusion of advection and turbulent diffusion, as well as influences on local gas temperature distributions are incorporated to account for cell size effects. These will feed back to the solid phase equations presented here. However, we can explore this concept by modifying the prescribed gas temperature distribution shown in Fig. 10. In these simulations, we assign a mean gas temperature of 500 K in the control volume and apply a range of variances for the moisture fraction 1 scenario under all 3 wind speed cases. The value indicated by x in ϕ_{gx} represents half the width of the top hat distribution, i.e., $500 + \phi_{gx}$ K is the maximum temperature in the top hat distribution with ϕ_{gx} ranging from 100 to 300 K. This figure highlights that increasing width of the gas temperature distribution results in an increase in width of the fuel temperature distribution in all wind cases, regardless of the state of combustion. Furthermore, increasing the wind speed

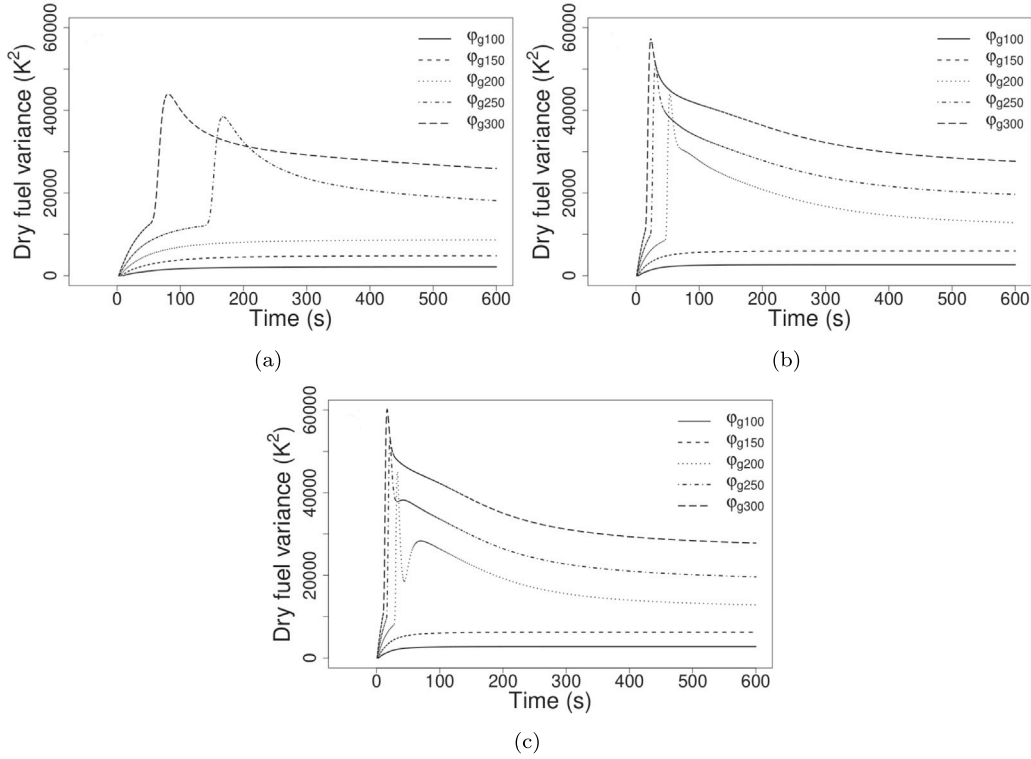


Fig. 10. Comparison of the effects for different gas temperature variances on the dry fuel variance for (a) 0.1 m s⁻¹, (b) 1.0 m s⁻¹ and (c) 2.0 m s⁻¹ winds. In all simulations the mean gas temperature is 500 K, the moisture fraction is 1 and ϕ_{gx} is a measure of the gas temperature variance, with x corresponding to the half the maximum width of the top hat.

(and thus convective heat transfer) increases dry fuel temperature variance in both combustion and non-combustion scenarios. This is because stronger convection will result in a stronger influence of the gas temperature on solid temperature.

Currently, FIRETEC simulations require significant computational resources on high performance computing systems due in part to restrictions on grid spacing. A single simulation in a small domain (e.g. 200 cells \times 200 cells \times 41 cells) requires tracking over 1.6 million cells, and within each of those cells computing or storing upwards of 40 variables at each time step with time steps as small as 0.001 s. Increasing the cell size has the potential to reduce computing requirements without compromising modeled fire behavior and will be examined in future work.

4.3. Field experiments and model comparison

On the afternoon of November 15, 2017 a series of experimental fires were conducted between 1700 and 1800 UTC on the University of Georgia campus providing data for the evaluation of the overall performance of the proposed model (Desai et al., 2021). For these experiments, the burn area was 2.4 \times 2.4 m and the fuel bed consisted of pine litter with a 4% moisture content and a fuel load of 0.37 kg m⁻² approximately 10 cm deep. The weather station recorded wind speeds of 0.635 and 0.474 m s⁻¹ at 1700 and 1800 UTC. Infrared and visual imagery were obtained using a Forward Looking Infrared SC660 thermal imaging system (FLIR Systems Inc., Boston, MA, USA) and a GoPro HERO3 mounted to a 7 m-tall aluminum tripod above the burn area facing downward. The FLIR system has a resolution of \approx 0.8 cm and a focal plane array of 640 \times 480 pixels at the 7 m distance. The temperature data was collected at 1 Hz for the range of 573 to 1773 K, and three different ignition patterns were completed: a point source, ring source, and 2 parallel lines. Four 1 \times 1 m cells were segregated for

each experimental fire and temperature distributions within each cell were analyzed at each second. Additional details can be found in Desai et al. (2021), Strother (2020).

Precise descriptions of the gas temperature and associated variance are unknown for these experiments. Given the lower intensity of the fire, we approximate the upwind gas temperature as $T_{g_{uwc}} = 300 + 500 \tanh\left(\frac{t-30}{100}\right) + 400 \tanh\left(\frac{400-t}{1000}\right)$, which allows for a slow gas temperature rise. The gas temperature variance, like the idealized scenarios previously discussed, is assigned as a function of temperature with a variance $\overline{T'_g T'_g} = \left(60 + \frac{\overline{T_g} - 300}{6}\right)^2$. Fuel bed temperature is initialized at 292 K and we estimate the ground level winds as $U = 0.6$ m s⁻¹, and TKE is assigned the same as described in Section 3 (which used for the mixing limited reaction rate) near ground.

The completed simulation compared to the observations is illustrated in Fig. 11, where the dashed lines are the mean temperatures of the various burning observations within the 1 \times 1 m cell, the red solid line with squares indicates modeled mean dry temperature, the blue solid line with circles is mean wet fuel temperature, the gray line is gas temperature and shading indicates one standard deviation above and below the mean based on the dry and wet modeled variances. The observed data is only presented for values above 773 K. Since there are multiple fire observations, we align the model data with the observations at peak temperatures. Furthermore, it is important to note that FLIR temperature observations are from the two-dimensional surface layer and do not capture variations in temperature below the surface. The proposed model, however, accounts for three-dimensional temperature distributions. With that said, unsurprisingly, the observed fuel temperatures are significantly hotter than the modeled mean temperatures. However, if we truncate the simulation data (from the modeled mean temperature and variance) to values in the distribution greater than 773 K, we observe a significant improvement in the alignment between modeled and observed temperature, especially after the

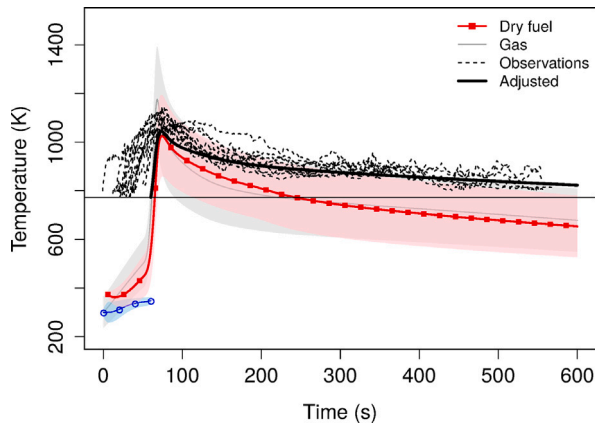


Fig. 11. Simulation results for the mean wet solid fuel, dry fuel and gas temperatures (blue, red, gray solid lines) compared with observations (dashed lines) of mean solid temperature evolution in a $1 \text{ m} \times 1 \text{ m}$ cell. The horizontal line is at 773 K (500 C) which is the minimum observed FLIR temperature. The adjusted dry fuel temperature (thick solid black line) is the recalculated mean temperature for temperatures above 773 K.

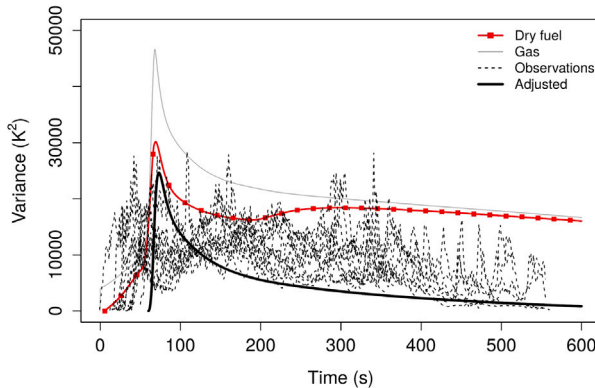


Fig. 12. Simulation results for modeled variance (solid line) compared with observations of variance in a $1 \text{ m} \times 1 \text{ m}$ cell. The adjusted variance is recalculated after removing all temperatures below 773 K, as discussed in Fig. 11.

peak temperature as shown by the solid black line. Distinct differences include a more rapid modeled rise in temperature during the initial combustion phase with a slightly premature drop in temperature as fuel is being consumed and a slower reaction rate. As previously discussed in the idealized scenarios, we hold the upwind gas temperature nearly constant with gradual increases and decreases. Thus, we are not capturing the turbulent gas temperature variations that would influence fire behavior. These limitations are not associated with the final model, but instead are the result of the overly simplified test cases presented here.

Fig. 12 illustrates the modeled variance and the observed variance. In this figure, the red solid line with squares is the modeled variance, the light gray line is the prescribed gas temperature variance and the dashed lines indicate the ensemble of variance observations. While the observed variances are approximately half to three-quarters of the modeled values (in red), this is not necessarily a case of overestimation by the modeled variance. Rather, it is the result of restricted range of observed temperatures measured by the FLIR. It is reasonable to assume that temperatures within a single cell solid would be below 500 C during a low-intensity fire, which is not accounted for in these observations. Thus, the results show fictitiously low variance. Furthermore, the three-dimensional distribution of temperatures, which are not accounted for in the FLIR observations, would further increase the

variance. This is because deeper fuel initially has lower temperatures compared to the surface temperature, which would be exposed to convective and radiant heating ahead of the flame front. As discussed in the previous figure with a mean temperature adjustment, we similarly observe a more realistic modeled variance by excluding fuels below 773 K. While magnitude of the modeled variance does not reflect the observed variance presented here, the overall shape and behavior of the variance aligns with the shape and behavior of the observed variance. Given the strong influence of the gas temperature variance on the fuel temperature variance, improvements to modeled gas temperature will improve the overall model performance.

4.4. Future work

The focus of this manuscript is on describing the governing equations for wet and dry fuels and their temperature evolution. Our future plan (currently ongoing) is to focus on the development of equations describing the evolution of the temperature variations for the gas phase based on a similar approach as described here. These new equations for the gas phase will then be coupled to the set of equations for the wet and dry fuels, which should improve the modeled energy exchange between wet and dry fuel and surrounding gas. This has a significant influence on fire behavior as we have previously shown. This energy exchange is one of the essential components contributing to the self-determining nature of FIRETEC. As such, considerable effort is being put toward these next developments.

Current assumptions neglecting triple correlation and higher order terms for multi-variable correlations are reasonable as a first approximation for this proof-of-concept discussion. Similarly, the assumed top hat distribution is physically unrealistic but allows us to remove many of the complications associated with an evolving distribution shape. However, future work will incorporate a more realistic probability distribution and return to the triple correlation terms that may have a non-negligible contribution. While a normal distribution in some cases is warranted, it cannot be assumed universally valid. As such, we are working towards capturing the sub-grid dynamic distribution changes over time. Next steps will also include triple correlations in the gas equation to account for skewness in the distribution. We recognize that the constants assigned initially in this study may be adjusted in future work. We anticipate that coupling a variable gas equation model to the solid fuel model described here will improve the convective heat transfer exchange and provide us with the opportunity to better evaluate and assign the constants c_h and $c_{T_d F}$. Thus, we will return to these constants in future studies.

Furthermore, while we currently apply a spatially segregated approach to the fine fuels (i.e., an individual fuel particle's moisture and temperature are always homogeneous, fuel is distributed evenly within the cell, and heating, cooling, evaporation and combustion can occur in a fraction of the cell leading to changes in the sub-grid temperature distributions), the current approach can be modified to a shell-type paradigm. In this new approach, fuel particles are initially heated on the outer layer, or shell, while the inner core of the particle may remain cool and wet. This new formation will allow gradients in fuel moisture and temperature, which is the first step towards the development of burning in thermally thick fuels and smoldering combustion; processes which are critically important to smoke and emissions production and many other fire effects.

5. Conclusion

A new model for the sub-grid processes related to temperature and moisture variation in wildfire behavior models is presented. Other wildfire behavior models have succeeded in simulating high-intensity fire during extreme conditions where the relevant length scales are large enough to be resolved and the impact of sub-grid variations is minimal. However, the performance of these models suffers when

conditions are less extreme and the length scales are small. The aim of the work described here is to improve the overall performance of these models, particularly during lower intensity fire where the sub-grid spatial and temporal variations have significant impacts on fire behavior.

The first set of simulations presented are idealized scenarios with prescribed upwind mean gas temperature, constant wind speed, and moisture content in the fuels. These simulations highlight the behavior of the model without the complex and non-linear effects of variations in wind speed and gas temperature. While we couple the fuel equations to an evolving gas temperature equation, the simplistic nature of the prescribed upwind gas temperature and the lack of cool air and overly simplified oxygen advection results in limitations on model performance. In nearly all simulations with combustion, an unnaturally rapid increase and decrease in temperature occurs as a result of this simplified advection. Aside from this deficiency, the model is able to effectively simulate the evolution of unresolved moisture and temperature and the resulting fuel consumption when conditions are both extreme and marginal. Furthermore, we illustrated the increased flexibility with respect to grid size in the proposed model through the influence of the gas equation with the dry fuel equation. We illustrated that wider variations in gas temperature directly result in wider variations in fuel temperature.

While we are unable to evaluate the performance of each term and closure in these new equations with observations, the overall behavior of the mean temperature and the variance equations is compared to a set of experimental burns conducted in 2017 at the University of Georgia. We present the results of a simulation using the known fuel load, moisture content, and approximate wind speed during these experimental fires for a 1 m × 1 m cell. The in-fire data is limited to temperatures above 773 K on the surface layer only, and so adjusting the model results to calculate the mean and variance in the fraction of modeled fuel hotter than 773 K is comparable to the observations. The major limitation of this comparison lies in the absence of modeled cool air entrainment, grossly simplified oxygen advection and the fact that observations are on a single plane but modeled temperature and fuel is 3 dimensional. Despite this, the model performs adequately.

This is the first step in ongoing work, which aims to couple the equations described here with new equations for the evolving gas temperature. This new coupled system of equations will ultimately be incorporated into the three-dimensional version of FIRETEC to improve the overall performance of the model, particularly during marginal burning conditions.

Declaration of competing interest

The authors declare that they have no known competing financial interests or personal relationships that could have appeared to influence the work reported in this paper.

Data availability

The authors do not have permission to share data.

Funding

This work was partially supported by the Strategic Environmental Research and Development Program, USA [Project Numbers RC-2643 & RC20-C3-1382]; and Los Alamos National Laboratory LDRD program, USA [project, 20220024DR Fighting Fire with Fire: Enabling a Proactive Approach to Wildland Fire].

References

- Accary, G., Meradji, S., Morvan, D., Bessonov, O., Fougère, D., 2014. FireStar3D: 3D finite volume model for the prediction of wildfires behaviour. In: Viegas, D.X. (Ed.), *Advances in Forest Fire Research*. Imprensa da Universidade de Coimbra, Coimbra, pp. 251–260. http://dx.doi.org/10.14195/978-989-26-0884-6_27.
- Aguado, I., Chuvieco, E., Boren, R., Nieto, H., 2007. Estimation of dead fuel moisture content from meteorological data in mediterranean areas. Applications in fire danger assessment. *Int. J. Wildland Fire* 16, 320–397. <http://dx.doi.org/10.1071/WF06136>.
- Banerjee, T., 2020. Impacts of forest thinning on wildland fire behavior. *Forests* 11 (9), <http://dx.doi.org/10.3390/F11090918>.
- Banerjee, T., Holland, T., Solander, K., Holmes, M., Linn, R., 2020. Identifying characteristics of wildfire towers and troughs. *Atmosphere* 11 (8), <http://dx.doi.org/10.3390/ATMOS11080796>.
- Besnard, D., Harlow, F.H., Rauen Zahn, R.M., Zemach, C., 1992. Turbulence transport equations for variable-density turbulence and their relationship to two-field models. Technical Report LA-12303-MS, Los Alamos National Laboratory.
- Byram, G.M., 1959. Combustion of forest fuels. In: Davis, K.P. (Ed.), *Forest Fire: Control and Use*. McGraw-Hill, New York, NY, pp. 61–89.
- Call, P., Albini, F., 1997. Aerial and surface fuel consumption in crown fires. *Int. J. Wildland Fire* 7 (3), 259–264. <http://dx.doi.org/10.1071/WF9970259>.
- Cheney, P., Sullivan, A., 2008. *Grassfires : Fuel, Weather and Fire Behaviour*, second ed. CSIRO Publishing, Collingwood, Australia.
- Clark, K.L., Heilman, W.E., Skowronski, N.S., Gallagher, M.R., Mueller, E., Hadden, R.M., Simeoni, A., 2020. Fire behavior, fuel consumption, and turbulence and energy exchange during prescribed fires in pitch pine forests. *Atmosphere* 11 (3), 242. <http://dx.doi.org/10.3390/atmos11030242>.
- Clements, C.B., Seto, D., 2015. Observations of fire-atmosphere interactions and near-surface heat transport on a slope. *Bound.-Layer. Meteorol.* 154 (3), 409–426. <http://dx.doi.org/10.1007/s10546-014-9982-7>.
- Clements, C.B., Zhong, S., Bian, X., Heidman, W.E., Byun, D.W., 2008. First observations of turbulence generated by grass fires. *J. Geophys. Res.: Atmos.* 113 (22), 1–13. <http://dx.doi.org/10.1029/2008JD010014>.
- Cohen, J.D., Finney, M.A., 2022a. Fuel particle heat transfer part 1: Convective cooling of irradiated fuel particles. *Combust. Sci. Technol.* 1–27. <http://dx.doi.org/10.1080/00102202.2021.2019231>.
- Cohen, J., Finney, M., 2022b. Fuel particle heat transfer part 2: Radiation and convection during spreading laboratory fires. *Combust. Sci. Technol.* 1–26. <http://dx.doi.org/10.1080/00102202.2021.2019232>.
- Daly, B.J., Harlow, F.H., 1970. Transport equations in turbulence. *Phys. Fluids* 13 (11), 2634–2649.
- de Groot, W.J., Hanes, C.C., Wang, Y., 2022. Crown fuel consumption in Canadian boreal forest fires. *Int. J. Wildland Fire* <http://dx.doi.org/10.1071/WF21049>.
- Desai, A., Goodrick, S., Banerjee, T., 2021. Investigating the turbulent dynamics of small-scale surface fires. *Earth Space Sci. Open Arch.* 28. <http://dx.doi.org/10.1002/essoar.10507823.1>.
- Drysdale, D., 1985. *An introduction to fire dynamics*. Wiley.
- Finney, M.A., Cohen, J.D., Forthofer, J.M., McAllister, S.S., Gollner, M.J., Gorham, D.J., Saito, K., Akafuah, N.K., Adam, B.A., English, J.D., Dickinson, R.E., 2015. Role of buoyant flame dynamics in wildfire spread. *Proc. Natl. Acad. Sci. USA* 112 (32), 9833–9838. <http://dx.doi.org/10.1073/pnas.1504498112>.
- Forestry Canada Fire Danger Group, 1992. Development and structure of the Canadian forest fire behavior prediction system. Tech. rep., Forestry Canada, Science and Sustainable Development Directorate: Ottawa, ON, Canada, 1992, Ottawa.
- Frangieh, N., Morvan, D., Meradji, S., Accary, G., Bessonov, O., 2018. Numerical simulation of grassland fires behavior using an implicit physical multiphase model. *Fire Saf. J.* 102, 37–47. <http://dx.doi.org/10.1016/j.firesaf.2018.06.004>.
- Hoffman, C.M., Canfield, J., Linn, R.R., Mell, W., Sieg, C.H., Pimont, F., Ziegler, J., 2016. Evaluating crown fire rate of spread predictions from physics-based models. *Fire Technol.* 52 (1), 221–237. <http://dx.doi.org/10.1007/s10694-015-0500-3>.
- Hoffman, C.M., Linn, R., Parsons, R., Sieg, C., Winterkamp, J., 2015. Modeling spatial and temporal dynamics of wind flow and potential fire behavior following a mountain pine beetle outbreak in a lodgepole pine forest. *Agricult. Forest Meteorol.* 204, 79–93. <http://dx.doi.org/10.1016/j.agrformet.2015.01.018>.
- Im, H.G., Lund, T.S., Ferziger, J.H., 1997. Large eddy simulation of turbulent front propagation with dynamic subgrid models. *Phys. Fluids* 9 (12), 3826–3833. <http://dx.doi.org/10.1063/1.869517>.
- Incropera, F.P., DeWitt, D.P., 1996. *Fundamentals of Heat and Mass Transfer*, fourth ed. John Wiley & Sons Inc., New York City, New York.
- Jeffrey, A. (Ed.), 1995. Chapter 13 - probability integrals and the error function. In: *Handbook of Mathematical Formulas and Integrals*. Academic Press, Boston, pp. 235–240.
- Jolly, W.M., Hadlow, A.M., Hugué, K., 2014. De-coupling seasonal changes in water content and dry matter to predict live conifer foliar moisture content. *Int. J. Wildland Fire* 23 (4), 480–489. <http://dx.doi.org/10.1071/WF13127>.
- Jonko, A.K., Yedinak, K.M., Conley, J.L., Linn, R.R., 2021. Sensitivity of grass fires burning in marginal conditions to atmospheric turbulence. *J. Geophys. Res.: Atmos.* 126 (13), <http://dx.doi.org/10.1029/2020JD033384>, e2020JD033384.

- Linn, R., 1997. A transport model for prediction of wildfire behavior. <http://dx.doi.org/10.2172/505313>.
- Linn, R.R., Cunningham, P., 2005a. Numerical simulations of grass fires using a coupled atmosphere-fire model: Basic fire behavior and dependence on wind speed. *J. Geophys. Res.: Atmos.* 110 (13), 1–19. <http://dx.doi.org/10.1029/2004JD005597>.
- Linn, R.R., Cunningham, P., 2005b. Numerical simulations of grass fires using a coupled atmosphere-fire model: Basic fire behavior and dependence on wind speed. *J. Geophys. Res.: Atmos.* 110 (13).
- Linn, R., Reisner, J., Colman, J.J., Winterkamp, J., 2002. Studying wildfire behavior using FIRETEC. *Int. J. Wildland Fire* 11 (4), 233–246. <http://dx.doi.org/10.1071/wf02007>.
- Linn, R.R., Winterkamp, J.L., Furman, J.H., Williams, B., Hiers, J.K., Jonko, A., O'Brien, J.J., Yedinak, K.M., Goodrick, S., 2021. Modeling low intensity fires: Lessons learned from 2012 RxCADRE. *Atmosphere* 12 (2), <http://dx.doi.org/10.3390/atmos12020139>.
- Marshall, G., Thompson, D., Anderson, K., Simpson, B., Linn, R., Schroeder, D., 2020. The impact of fuel treatments on wildfire behavior in north american boreal fuels: A simulation study using FIRETEC. *Fire* 3 (2), 1–14. <http://dx.doi.org/10.3390/fire3020018>.
- Martell, D.L., 2001. *Forest Fire Management*. In: Johnson, E.A., Miyanishi, K. (Eds.), *Forest Fires: Behaviour and Ecological Effects*. Academic Press, San Diego, pp. 527–583.
- Mell, W., Jenkins, M.A., Gould, J., Cheney, P., 2007. A physics-based approach to modelling grassland fires. *Int. J. Wildland Fire* 16, 1–22. <http://dx.doi.org/10.1071/WF06002>.
- Mell, W., Maranghides, A., McDermott, R., Manzello, S.L., 2009. Numerical simulation and experiments of burning douglas fir trees. *Combust. Flame* 156 (10), 2023–2041. <http://dx.doi.org/10.1016/j.combustflame.2009.06.015>.
- Morvan, D., Accary, G., Meradji, S., Frangieh, N., Bessonov, O., 2018. A 3D physical model to study the behaviour of vegetation fires at laboratory scale. *Fire Saf. J.* 101, <http://dx.doi.org/10.1016/j.firesaf.2018.08.011>.
- Parsons, R.A., Mell, W.E., McCauley, P., 2011. Linking 3D spatial models of fuels and fire: Effects of spatial heterogeneity on fire behavior. *Ecol. Model.* 222 (3), 679–691. <http://dx.doi.org/10.1016/j.ecolmodel.2010.10.023>.
- Potter, B.E., McEvoy, D., 2021. Weather factors associated with extremely large fires and fire growth days. *Earth Interact.* 25 (1), 160–176. <http://dx.doi.org/10.1175/EI-D-21-0008.1>.
- Seto, D., Clements, C.B., Heilman, W.E., 2013. Turbulence spectra measured during fire front passage. *Agricult. Forest Meteorol.* 169, 195–210. <http://dx.doi.org/10.1016/j.agrformet.2012.09.015>.
- Stocks, B.J., Alexander, M.E., Wotton, B.M., Steffner, C.N., Flannigan, M.D., Taylor, S.W., Lavoie, N., Mason, J.A., Hartley, G.R., Maffey, M.E., Dalrymple, G.N., Blake, T.W., Cruz, M.G., Lanoville, R.A., 2004. Crown fire behaviour in a northern jack pine - Black spruce forest. *Can. J. Forest Res.* 34 (8), 1548–1560. <http://dx.doi.org/10.1139/X04-054>.
- Strother, D., 2020. *The Role of Black Carbon in a Longleaf Pine Ecosystem* (Ph.D. thesis). University of Georgia, p. 93.
- Sullivan, A.L., 2009. Wildland surface fire spread modelling, 1990–2007.1: Physical and quasi-physical models. *Int. J. Wildland Fire* 8, 349–368. <http://dx.doi.org/10.1071/WF06143>.
- Taylor, S.W., Wotton, B.M., Alexander, M.E., Dalrymple, G.N., 2004. Variation in wind and crown fire behaviour in a northern jack pine - Black spruce forest. *Can. J. Forest Res.* 34 (8), 1561–1576. <http://dx.doi.org/10.1139/X04-116>.
- Thompson, D.K., Schroeder, D., Wilkinson, S.L., Barber, Q., Baxter, G., Cameron, H., Hsieh, R., Marshall, G., Moore, B., Refai, R., Rodell, C., Schiks, T., Verkaik, G.J., Zerb, J., 2020. Recent crown thinning in a boreal black spruce forest does not reduce spread rate nor total fuel consumption: Results from an experimental crown fire in Alberta, Canada. *Fire* 3 (3), <http://dx.doi.org/10.3390/fire3030028>.
- van der Kamp, D., Moore, R., McKendry, I., 2017. A model for simulating the moisture content of standardized fuel sticks of various sizes. *Agricult. Forest Meteorol.* 236, 123–134. <http://dx.doi.org/10.1016/j.agrformet.2017.01.013>.
- Veynante, D., Vervisch, L., 2002. Turbulent combustion modeling. *Prog. Energy Combust. Sci.* 28 (3), 193–266. [http://dx.doi.org/10.1016/S0360-1285\(01\)00017-X](http://dx.doi.org/10.1016/S0360-1285(01)00017-X).
- Wotton, B.M., Gould, J.S., McCaw, W.L., Cheney, N.P., Taylor, S.W., 2012. Flame temperature and residence time of fires in dry eucalypt forest. *Int. J. Wildland Fire* 21 (3), 270–281. <http://dx.doi.org/10.1071/WF10127>.
- Zhou, X., Mahalingam, S., Weise, D., 2005. Modeling of marginal burning state of fire spread in live chaparral shrub fuel bed. *Combust. Flame* 143 (3), 183–198. <http://dx.doi.org/10.1016/j.combustflame.2005.05.013>.